密度汎関数理論に基づく、ガラス転移及びそのメカニズムに対する基礎研究

AUTHOR(S):

宗像, 豊哲

密度汎関数理論に基づく、ガラス転移及びそのメカニズムに関する基礎研究

(研究課題番号 12650063)

平成12年度～平成13年度科学研究費補助金
(基盤研究 (C)(2))
研究成果報告書

平成13年3月
研究代表者 宗像豊哲
(京都大学情報学研究科教授)

密度汎関数理論に基づく、ガラス転移及びそのメカニズムに関する基礎研究

(研究課題番号 12650063)

平成12年度～平成13年度科学研究費補助金
(基盤研究 (C)(2))
研究成果報告書

平成13年3月

研究代表者 宗像豊哲
(京都大学情報学研究科教授)

はしがき

この報告書は、平成12年度から平成13年度までの2年間にわたって、学術振興会科学研究費補助金(基盤研究(C)(2))を得て行なわれた次の研究の成果をまとめたものである。

課題番号

12650063

研究課題

密度汎関数理論に基づく、ガラス転移及びそのメカニズムに関する基礎研究

研究組織

研究代表者 ： 宗像豊哲 (京都大学情報学研究科教授)

研究経費

平成12年度 2、400千円

平成13年度 1、100千円

計 3、500千円

研究発表

(1)学会誌等

1. T. Munakata and K. Kim
M-body Density Functional Theory and Generalized Hypernetted-Chain Equation
J. Chem. Phys. **113** (2000) 3975-3979.

2. H. Okamoto, A. Igarashi and T. Munakata
Dynamical Properties of a Low-dimensional Chaotic Reservor
J. Phys. Soc. Japan **69** (2000) 3481-3484.

3. T. Munakata:
Density Functional Theory of Liquids, Some Extensions and Applications
J. Mol. Liq. **90** (2001) 205-214

4. T. Munakata and Y. Nakamura:
Temperature Control for Simulated Annealing
Phys. Rev. E **64** (2001) 046127. (1-5)

5. T.Munakata and H. Ogawa
Dynamical Aspects of an adiabatic Piston
Phys. Rev. E **64** (2001) 036119. (1-4)

6. 宗像豊哲、 金 鋼
過冷却液体の構造
原子力研究所「 ガラス・過冷却液体の物性： 理論と実験の接点を求めて」報告書

現在投稿中のもの
7. T. Munakata and Gang Hu
Statistical Mechanics of Two Hard Disks in a Rectangular Box
Phys. Rev. submitted.

8. Kang Kim and T. Munakata
Three-body hypernetted-chain equation and its numerical solution
J. Chem. Phys. submitted

(2) 口頭発表

1. 宗像豊哲、 金 鋼
M 次密度汎関数理論と一般化 HNC 理論 II
物理学会 2000 年春の分科会（於 関西大学 2000 年 3 月 22 日）

2. 宗像豊哲、中村泰之、 池本真吾
simulated annealing と温度制御（変分アプローチ）
物理学会 2000 年秋の分科会（於 新潟大学、2000 年 9 月 22 日）

3. 宗像豊哲, 小川英輝
断熱ピストンの運動と緩和
物理学会 2001 年年会 （於 中央大学多摩キャンパス、2001 年 3 月 27 日）

4. 宗像豊哲, Gang Hu(Beijin Normal University)
Statistical Mechanics of Two Hard Disks in a Rectangular Box
物理学会 2001 年春の分科会（於 立命館大学、2001 年 3 月 26 日)

5. 宗像豊哲、 金 鋼
過冷却液体の構造ー分子動力学と密度汎関数理論
原子力研究所研究会（2000 年 10 月 5 日）
「 ガラス・過冷却液体の物性： 理論と実験の接点を求めて」

(3) 出版物

なし

研究成果

目次

1. T. Munakata and K. Kim
M-body Density Functional Theory and Generalized Hypernetted-Chain Equation
J. Chem. Phys. **113** (2000) 3975-3979.

2. H. Okamoto, A. Igarashi and T. Munakata
Dynamical Properties of a Low-dimensional Chaotic Reservor
J. Phys. Soc. Japan **69** (2000) 3481-3484.

3. T. Munakata:
Density Functional Theory of Liquids, Some Extensions and Applications
J. Mol. Liq. **90** (2001) 205-214

4. T. Munakata and Y. Nakamura:
Temperature Control for Simulated Annealing
Phys. Rev. E **64** (2001) 046127. (1-5)

5. T.Munakata and H. Ogawa
Dynamical Aspects of an adiabatic Piston
Phys. Rev. E **64** (2001) 036119. (1-4)

6. 宗像豊哲、 金 鋼
過冷却液体の構造
原子力研究所「 ガラス・過冷却液体の物性： 理論と実験の接点を求めて」報告書

現在投稿中のもの
7. T. Munakata and Gang Hu
Statistical Mechanics of Two Hard Disks in a Rectangular Box
Phys. Rev. submitted.

8. Kang Kim and T. Munakata
Three-body hypernetted-chain equation and its numerical solution
J. Chem. Phys. submitted

(1) 本研究の背景

1970年代から世界的に広まった、中性子・光散乱実験や計算機実験による精力的な研究により、これまで液体のミクロな構造（主として2体相関）や動力学（時間相関関数や輸送係数）についての知見が集積・深化し、これに伴い種々のモデル系に対する理論が統計力学や力学系理論を用いて展開されてきた。液体研究のこの流れは近年2つの方向へと発展・分化した。1つは複雑液体の研究であり、他はより高密度な過冷却液体・ガラス転移の研究である。我々は特に後者の問題に長年興味をもち、研究に取り組んでいる。

ガラス（転移）はここ10年以上非常にhotな分野である。基礎的な側面からは、従来の比熱等、熱測定に基づく実験に加えて、中性子・光（非）弾性散乱、スピンエコー法等を用いた新しい手段によりメソスコピックな領域の構造・緩和に関する多くの興味ある知見が得られ、その基礎的、理論的な理解・解明が重要課題として認識されたことによるが、またイオンガラス、(生体）高分子ガラス等の物性解明や応用的な（バッテリー等）側面にも関心が集まっている。

本研究の目的は（過冷却）液体系の示す**ガラス転移**及びそれを引き起こす**メカニズム**を微視的な理論、特に**密度汎関数理論（DFT）**の立場から解明することである。と同時に、計算機実験のグループとの共同研究により、過冷却液体内で生起している種々の動的な過程を明らかにし、それに理論的な縦糸を通すことである。　具体的には次の4点について研究した。:

- 密度汎関数理論による過冷却液体の構造、特に高次相関関数の解明：

高密度系では従来の積分方程式は構造に対して実験（含 計算機実験）とかなりずれる結果を与える。そこでこれまで用いられてきた2次のDFTに代る、高次のDFTの開発とそれから導かれる改良された積分方程式理論（高次hyper-netted chain（HNC) 理論）の展開を図った。これにより高密度液体の構造を精確かつ定量的に扱い、ガラス転移に対する前駆現象としての構造変化（2体相関）とcage-effect, 集団運動（3次及び高次相関）を明らかにする準備ができた。具体的には従来の2体理論から決別し、*M-body density functional theory* を定式化した。数値計算を1次元系に対してM＝3の場合に実行した（3体理論)。今回、繰り返し計算の収束を実現し、また結果を計算機実験に比較すると、従来のHNCを大きく改善していることを確認できた。

- ガラス転移点近傍での動特性、特に密度緩和と空間非一様性の研究：

ガラス状態を液体状態の凝固と考えると、この原因として拡散係数の低下、及び粘性係数の増大によるslowing downがある。動的なDFT（D-DFT）を用いてこれらの輸送係数の定量的な予言を行う計算は密度場が負になるという困難に直面した。ことため、計算機実験による新しい実験を提案し実行した。すなわち、非一様な領域あるいは動的な相関領域(dynamically correlated region) のサイズについて、定量的な結果を得るために、分子動力学での計算の途中に幾つかの粒子を空間固定し、これにより生成された非一様性の性質からサイズについてこれが温度の逆数の冪で大きくなることをしめした。これについては2002年春の学会で発表予定であると同時に原子力研究所での研究会においてプレリミナリーな結果を発表している。

- 閉じ込められた系（confined system）と相転移：

最近注目されているconfined systemについて、若干人為的ではあるが、長方形の容器に閉じ込められた2つの剛体円盤の統計力学について考察した。2体問題ではあるが、周期境界条件を使用しないことから強烈な非一様性が生じ、これによりファンデルワールス

の不安定性が作られ、液相ー気相転移が起る。ガラスは非常に非一様性が強く、多くのconfined systems あるいは confined structures の寄せ集めというイメージがあり、別の見方としては2準位系の集合とした取り扱いが古くからあるが、我々の研究はこれらに対して新しい観点を提供している。

● 密度汎関数理論の動的な拡張：

従来の密度汎関数理論の動的な拡張というアプローチではなく、全く新しい射影演算子の理論（森ー藤坂理論）を応用した、動的な理論を展開した。密度場の動力学を支配するランジェバン方程式はこれまでのものと同一であるが、自由エネルギー汎関数が密度汎関数理論に拠るものと違っており、この方向での大きな進展が期待される。これについては予備的な成果を原子力研究所でのガラス転移の研究会で発表した。

(2) 本研究での研究成果

(i) 研究成果の概要

(A) 密度汎関数理論による過冷却液体の構造、特に高次相関関数の解明：
非一様な液体系の統計力学理論として密度汎関数理論は重要な役割をはたしてきた。特に固体ー液体相転移、固体ー液体界面、非晶質、核形成の問題等において多くの研究者により応用されている。これにはDFTのもつ物理的な簡明さと計算の単純さが寄与していると考えられる。DFTの一般性と応用面での単純さに鑑み、我々はこれを
- 静的な拡張としては、M体DFTを提案し、理論的にもその有用性を確認した。（文献1、3、8参照）また
- 動的な拡張としては、射影演算子を用いて全く新しい動的なDFTを提案した。これは従来の動的なDFTに対する批判に完全に答えており、統計力学的にも正しい導出になっている。これの応用に関しては今後とも引き続き研究をする予定である。（文献6参照）

(B) 動的な相関領域と計算機実験
理論及び実験両サイドから過冷却液体の構造に関して、非一様な領域あるいは動的な相関領域(dynamically correlated region)が注目されている。そのサイズについて、定量的な結果を得るために、分子動力学での計算の途中に幾つかの粒子を空間固定し、これにより生成された非一様性の性質からサイズについてこれが温度の逆数の冪で大きくなることをしめした。(2002年物理学会春の分化会で発表予定)

(C) 閉じ込められた系（confined system）と相転移：
表面や多孔性媒質等では、物質はある限られた領域に閉じ込められており、種々のおもしろい性質を示す。これら空間的にconfinedされた系について、少数体モデルを提案しそこでの厳密な統計力学を展開した。少数体であっても、閉じ込められた系ではファンデルワールスの不安定性を示し、エルゴードー非エルゴード転移に伴い液相ー気相転移と呼べるものが存在することを明らかにした。（文献7参照）

（D）その他の関連する研究
相転移を力学系の理論から理解しようというアイデアは古くからあり、特にカオスとの関連で興味深いテーマーである。文献2ではこの線に沿い、カオスと熱浴の関連を調べている。また温度制御はガラスの問題で重要であるが、とくにsimulated annealingにおける温度のコントロールについて文献4で研究した。また文献5では断熱ピストンの振る舞いを確率過程として捉え、マスター方程式を用いて解明した。

(ii) 印刷物

M-body density functional theory and the generalized hypernetted-chain equation

Toyonori Munakata[a] and Kang Kim
Department of Applied Mathematics and Physics, Kyoto University, Kyoto 606, Japan

(Received 12 October 1999; accepted 16 June 2000)

The HNC (hypernetted-chain) theory for two-body correlation in fluids is generalized so that up to M-body ($M>2$) correlation functions can be obtained self-consistently. Our approach is based on the M-body density functional theory and a generalized Percus idea where maximally $M-1$ particles are held fixed in space, leading to $M-1$ HNC equations for the correlation functions. These are supplemented with $M-1$ Ornstein–Zernike relations to give a closed set of equations. Due to the rather complicated structure of the coupled integral equations, we explicitly present the equations for the case $M=3$, which are compared with the HNC2 equations by Verlet. The $M=3$ theory is numerically solved for the case of a one-dimensional liquid. © *2000 American Institute of Physics.* [S0021-9606(00)51934-5]

I. INTRODUCTION

The density functional theory (DFT) of nonuniform fluids has been playing an important role in classical many-body theory.[1] It has been successfully applied in quantitative studies on solid–liquid transformations, including interfacial and nucleation phenomena, and so on.[2] Recently the DFT has been extended in various ways, e.g., to investigate molecular systems[3] and dynamic aspects of various phenomena mentioned previously.[4]

It is remarked here that the DFT is closely related to the equilibrium theory for structure of uniform fluids.[5] That is, if one has a reliable expression or approximation for the free-energy density functional $F[n(\boldsymbol{r})]$, with $n(\boldsymbol{r})$ denoting a density field for a fluid, one can derive a good equation for the radial distribution function $g_2(r)=1+h_2(r)$ which represents two-body correlations in a fluid.

To illustrate this interconnection, we consider a simple d-dimensional liquid with interparticle interaction $\phi(r)$. First let us hold, following Percus,[6] a particle fixed at the origin of the coordinate system. Then the (equilibrium) density $n(\boldsymbol{r})$, which obeys the variational Eq. (1), just represents $n_0 g_2(r)$ with n_0 being the uniform density,

$$\delta F/\delta n(\boldsymbol{r})+\phi(r)=\mu, \tag{1}$$

with μ a chemical potential. The two-body approximation for $F[n(\boldsymbol{r})]$ is given by[1,2]

$$\begin{aligned} F_2[n] &= k_B T\int d\boldsymbol{r}\, n(\boldsymbol{r})\ln[n(\boldsymbol{r})\Lambda^d] \\ &\quad -(k_B T/2)\int d\boldsymbol{r}\int d\boldsymbol{r}'\ \delta n(\boldsymbol{r})c_2(|\boldsymbol{r}-\boldsymbol{r}'|)\,\delta n(\boldsymbol{r}') \\ &\equiv F_{\mathrm{id}}+F_{\mathrm{ex}}^{(2)}, \end{aligned} \tag{2}$$

where Λ is the thermal wavelength and $\delta n(\boldsymbol{r})\equiv n(\boldsymbol{r})-n_0$. F_{id} and $F_{\mathrm{ex}}^{(2)}$ denote the ideal gas part and the two-body contribution to the excess part, respectively. The two-body direct correlation function $c_2(r)$ multiplied by $-k_B T$ is seen to represent an effective interaction. The $c_2(r)$ is related to the two-body total correlation function $h_2(r)\equiv g_2(r)-1$ via an exact two-body Ornstein–Zernike equation,[5]

$$\begin{aligned} h_2(r) &= c_2(r)+n_0\int d\boldsymbol{r}\, h_2(|\boldsymbol{r}-\boldsymbol{r}'|)c_2(r') \\ &\equiv c_2(r)+n_0 h_2 * c_2(r). \end{aligned} \tag{3}$$

Inserting Eq. (2) into the variational equation (1) and taking into account the fact that $n(\boldsymbol{r})=n_0 g_2(r)$ is normalized to n_0 at infinity or $g_2(r\to\infty)=1$, we immediately obtain the (two-body) hypernetted-chain (HNC) equation

$$\ln g_2(r)=-[\phi(r)-n_0 k_B T h_2 * c_2(r)]/(k_B T). \tag{4}$$

Thus we have two equations, (3) and (4), for the two unknowns $c_2(r)$ and $g_2(r)$. The terms in the square brackets on the right-hand side of Eq. (4) express the potential field felt by a particle at $\boldsymbol{r}$. The first term represents the direct field produced by a particle put at the origin and the second the indirect one produced by the surrounding particles.

The HNC equation has been applied to many kinds of fluids to study their structures and turned out to be very useful for theoretical prediction of $g_2(r)$ up to the density slightly lower than that at the freezing point.[5] It is noted in passing that the HNC theory was first derived not based on the DFT theory but on some mathematical or diagrammatical argument.[5,7] However, the physical and concise DFT approach just presented suggests that we can rather straightforwardly extend the two-body HNC theory to higher order ones and this is what we try to do in this paper.

In Sec. II we develop a general M-body HNC theory based on the DFT. In Sec. III we investigate the case $M=3$ by explicitly writing down the closed set of equations for two- and three-body correlation functions. This is first compared with another extension of the HNC theory, i.e., the HNC2 by Verlet,[8] and the virial coefficients are discussed. The $M=3$ theory is then solved numerically for a one-

[a]Electronic mail: munakatakuamp.kyoto-u.ac.jp

dimensional liquid and some preliminary results for two- and three-body correlations are presented. Finally in Sec. IV we conclude the paper with some remarks.

II. *M*-BODY HNC THEORY

Let us generalize the argument to derive the HNC equation (4) and establish a theory to deal with (up to) M-body ($M>2$) correlation functions self-consistently. For this purpose we approximate F_{ex} by including up to the M-th order terms as

$$F_{ex}[n] \simeq \sum_{2}^{M} F_{ex}^{(j)}[n], \tag{5}$$

where $F_{ex}^{(j)}[n]$ contains the jth order direct correlation function $c_j(1,2,..,j)$ with 1 denoting $\boldsymbol{r}_1$. Thus explicitly we have, e.g.,[1,2]

$$F_{ex}^{(j)}[n] = -(k_BT/j!)\int d1 \cdots \int dj\, c_j(1,2,\ldots,j) \times \delta n(1)\cdots\delta n(j). \tag{6}$$

The first step of our M-body HNC theory is to notice that for the M-body correlation function $g_M(1,..,M)$, which is normalized to unity at infinity, we have

$$\begin{aligned} g_M(1,\ldots,M) &= g_{M-1}(1,\ldots,M-1)g_1(M|1,\ldots,M-1) \\ &= g_1(2|1)g_1(3|1,2)g_1(4|1,2,3)\cdots \\ &\quad g_1(M|1,2,\ldots,M-1), \end{aligned} \tag{7}$$

where, for example, $n_0 g_1(4|1,2,3)$ represents a one-body distribution function at 4 when three particles are located at 1,2, and 3. If M points $\{1,2,\ldots,M\}$ are regarded as points on a time axis, Eq. (7) reminds us of a non-Markovian stochastic process.[9] Furthermore this non-Markovian property is similar in its origin to that in the random-walk interpretation of polymer conformation (the excluded volume effect).[10]

Assuming that $c_j(1,\ldots,j)(j=2,\ldots,M)$ are known, we follow the idea of Percus[6] (this time however, maximally $M-1$ particles are held fixed in space) to derive an equation for $\ln g_1(j|1,2,\ldots,j-1)(j=2,\ldots,M)$, based on Eqs. (1), (5), and (6) and the fact that the external field appearing on the left-hand side of the variational equation (1) is the sum of the field produced by particles located at 1, 2,..., and $j-1$. From this we readily obtain

$$\ln g_1(j|1,2,\ldots,j-1) = -\sum_{i=1}^{j-1} \phi(i,j)/(k_BT) + \Gamma_j^M[g_1(j|1,2,\ldots,j-1)-1], \tag{8}$$

$$\Gamma_j^M[f] \equiv \sum_{i=2}^{M} [n_0^{i-1}/(i-1)!]\int d1' \cdots \int d(i-1)' \times c_i(1',2',\ldots,(i-1)',j) f(1')\ldots f((i-1)'), \tag{9}$$

where $f(1') \equiv g_1(1'|1,2,\ldots,j-1)-1$. Thus we have $m-1$ equations, Eq. (8) $(j=2,\ldots,M)$ for $M-1$ unknowns $g_1(j|1,2,\ldots,j-1)(j=2,\ldots,M)$.

As to the direct correlation functions, which were assumed to be known previously, we know that they are in a sense inverse functions of the correlation functions[2,3,5] and $c_j(1,2,\ldots,j)$ can be expressed in terms of $g_k(1,2,\ldots,k)\times(k=2,3,\ldots,j)$. This relation may be called the j-body Ornstein–Zernike relation. Thus in principle we have $M-1$ relations between $c_j(1,\ldots,j)(j=2,\ldots,M)$ and $g_j(1,\ldots,j)(j=2,\ldots,M)$ and these complete the M-body HNC theory.

III. THREE-BODY HNC THEORY

A. Structure of three-body HNC equation

For concreteness and later convenience we write down explicitly the set of equations to determine $g_2(1,2)$ and $g_3(1,2,3)$ for the case $M=3$. First, Eq. (7) takes the form

$$g_3(1,2,3) = g_1(2|1)g_1(3|1,2), \tag{10}$$

where $g_1(2|1)$ is nothing but the two-body radial distribution function $g_2(1,2)$. The HNC Eq. (8) for $M=3$ is

$$\begin{aligned} \ln g_1(2|1) &= -\phi(1,2)/(k_BT) + n_0\int d1' c_2(1',2) h_1(1'|1) \\ &\quad + (n_0^2/2) \times \int d1' d2' c_3(1',2',2) h_1(1'|1) h(2'|1) \\ &= -\phi(1,2)/(k_BT) + C^{(2)} + B^{(2)}, \end{aligned} \tag{11}$$

$$\begin{aligned} \ln g_1(3|1,2) &= -(k_BT)^{-1}(\phi(2,3)+\phi(1,3)) \\ &\quad + n_0\int d1' c_2(1',3) h_1(1'|1,2) + (n_0^2/2) \\ &\quad \times \int d1' \int d2' c(1',2',3) \\ &\quad \times h_1(1'|1,2) h_1(2'|1,2) \\ &= -(k_BT)^{-1}(\phi(2,3)+\phi(1,3)) + C^{(3)} + B^{(3)}, \end{aligned} \tag{12}$$

where $h_1(2|1) \equiv g_1(2|1)-1$ and $h_1(1|2,3) \equiv g_1(1|2,3)-1$. Comparing Eq. (11) with Eq. (4), we see that we have an extra contribution $B^{(2)}$, representing the potential field at 2 produced by particles at 1' and 2' through the (effective) three-body interaction c_3. This corresponds to the bridge function, which is neglected in the usual (two-body) HNC approximation.[5]

We now turn to the functions c_2 and c_3, which are related to g_2 and g_3 through the Ornstein–Zernike (OZ) relations. The two- and three-body Ornstein–Zernike relations are most concisely expressed in terms of Fourier transformation as

$$\hat{h}_2(q) = \hat{c}_2(q)(1+n_0\hat{h}_2(q)), \tag{13}$$

$$\hat{H}(\boldsymbol{q}_1,\boldsymbol{q}_2)=\hat{c}_3(\boldsymbol{q}_1,\boldsymbol{q}_2)G(\boldsymbol{q}_1,\boldsymbol{q}_2), \tag{14}$$

where $G(\boldsymbol{q}_1,\boldsymbol{q}_2))\equiv(1+n_0\hat{h}_2(q_1))(1+n_0\hat{h}_2(q_2))(1+n_0\hat{h}_2\times(|\boldsymbol{q}_1+\boldsymbol{q}_2|))$ and $\hat{c}_3(\boldsymbol{q}_1,\boldsymbol{q}_2)$ denotes the Fourier transform of $c_3(1,2,3)$ with 3 taken to be the origin of the coordinate system. Similarly $\hat{H}(\boldsymbol{q}_1,\boldsymbol{q}_2)$ in Eq. (14) is defined as the Fourier transform of

$$\begin{aligned}H(1,2,3)\equiv& h_3(1,2,3)-h_2(1,2)-h_2(2,3)-h_2(1,3)\\&-n_0\int d4h_2(1,4)h_2(2,4)h_2(3,4)\\&-[h_2(1,2)h_2(2,3)+h_2(1,3)h_2(3,2)\\&+h_2(2,1)h_2(1,3)],\end{aligned} \tag{15}$$

with $h_3(1,2,3)\equiv g_3(1,2,3)-1$. In summary we have now four integral equations—(11), (12), (14), and (15)—for four unknowns c_2,c_3,g_2, and g_3 or $g(3|1,2)$ supplemented by Eq. (10).

Before proceeding to numerical analysis of the case $M=3$, we briefly comment on the HNC2 equation[8] by Verlet, who extended the (functional) expansion method due to Percus[6] to explicitly include effects of three-body correlations. The HNC2 equation consists of Eq. (11) for the two-body correlation function and Eq. (12) without the $B^{(3)}$ term for the three-body correlation function. As to the virial coefficients $\{V_n\}$[5] it gives the exact result up to fourth order (HNC is exact up to third order) and V_5 for the hard sphere system from the HNC2 is 0.122 although the exact one is 0.11 and the superposition approximation (SA) gives 0.16.[8] Later we comment on the SA from the viewpoint of the $M=3$ HNC theory. The contribution of $B^{(3)}$ in Eq. (12) to the virial coefficients appears first at V_6, so our $M=3$ theory and HNC2 give identical results as to V_5.

B. Numerical study of the $M=3$ HNC theory

Looking at Eqs. (11) and (12) we immediately notice that Eq. (12) has a similar structure to that of Eq. (11). The difference comes from the fact that for Eq. (12) two particles are held fixed at 1 and 2, thus yielding two ϕ terms and h_1 function depending on two variables—1 and 2—in contrast to one ϕ term and one variable 1 for Eq. (11). Setting the variable 1 in Eqs. (11) and (12) equal to the zero vector (the origin of the coordinate), we still have one variable "2" for Eq. (12), which is regarded as a parameter of Eq. (12). That is, Eq. (12) has to be solved for each value of the variable 2. In view of the similarity in structure of the HNC equations (11) and (12) with the two-body HNC equation (4), we employ the following procedure to solve the $M=3$ theory: Starting from a trial (as to the first step, the ideal gas) direct correlation functions c_m^{tr} $(m=2,3)$, we calculate new ones c_m^{new} $(m=2,3)$. Then the new trial functions are taken to be a linear combination as

$$c_m^{\mathrm{tr,new}}=(1-w_m^{\mathrm{new}})c_m^{\mathrm{tr}}+w_m^{\mathrm{new}}c_m^{\mathrm{new}} \quad (m=2,3), \tag{16}$$

with w_m^{new} $(m=2,3)$ denoting the weight for the new ones.[5] This constitutes one iteration, which consists of three steps. First, we calculate h_1 functions on the right-hand side of Eqs. (11) and (12) based on the OZ equations (13) and (14) from c_2^{tr} and c_3^{tr}. Second, we make use of the HNC equations (11) and (12) to have new h_1 functions. Finally, we calculate c_2^{new} and c_3^{new} functions from the new h_1 functions, which is the opposite of the first step, and use Eq. (16) for new trial functions.

Numerical calculation was performed for a one-dimensional soft-rod system with $\phi(r)=\epsilon(\sigma/r)$.[12] A thermodynamic state of the system is characterized by one variable, which we take to be the nondimensional temperature $T^*\equiv(k_BT/\epsilon)(l/\sigma)^{12}$ with $l\equiv 1/n_0$. One iteration mentioned previously took more than 10 min for our workstation but if we neglect the $B^{(3)}$ term in Eq. (12), that is for HNC2, it took about 5 min or less for one iteration. For a one-dimensional system the two-body correlation function $h_2(x)=g_2(x)-1$ shows strong oscillatory behavior at low (high) temperature (density). In this case the correlation becomes long-ranged and the memory required for numerical calculations becomes large. One reason for our studying a one-dimensional system is the memory conservation and we consider the case $T^*=5000$ only, where $h_2(x)$ is moderately oscillatory.

Here it is worthwhile to comment briefly on the convergence of iterative calculations. In the iteration step convergence is judged based on how the norm $N_m\equiv\|c_m^{\mathrm{new}}-c_m^{\mathrm{tr}}\|$ $(m=2,3)$ changes as an iteration number increases. For HNC2 a weight $w_m^{\mathrm{new}}=0.5$ $(m=2,3)$ in Eq. (16) worked well to attain convergence and we obtained rather oscillatory $h_2(x)$ (several peaks are discernible), which corresponds to the structure with lower T^*. For $M=3$ HNC, this weight does not work and we chose tentatively $w_m^{\mathrm{new}}=0.1$ $(m=2,3)$ and the numerical results shown in the following are obtained at about 100 iterations. (After this the norm N_3 began to increase slowly.) In this connection we note that fine tuning, which uses different values for w_2^{new} and w_3^{new}, may be necessary and this is left for future study.

In Fig. 1 we compare $h_2(x)$ from numerical experiments ($x>0$, a solid curve) and $M=3$ ($x<0$, a solid curve) theory with that from the usual ($M=2$) HNC theory (a dotted curve). As is well known[5] and observed in Fig. 1, the $M=2$ theory predicts a higher first peak and a more compressed structure compared with the experimental one. Our numerical solution to $M=3$ HNC equations is seen to be similar to the $M=2$ HNC results, with minor improvement in peak heights and positions. In Fig. 2 the $C^{(2)}(x)$ (a solid curve) and $10\times B^{(2)}(x)$ (a dotted curve) are plotted. Although $B^{(2)}$ is considerably smaller than $C^{(2)}$ at this temperature, its effect on the phase relation (i.e., peak and valley positions) is seen to be in the right direction.

One advantage of the $M=3$ theory is that various three-body correlations are obtained self-consistently. We depict in Fig. 3(a) $C^{(3)}(x|y,z)$(a dotted curve) and $C_{SA}^{(3)}(x|y,z)\equiv C^{(2)}(x|y)+C^{(2)}(x|z)$ (a solid curve) and in Fig. 3(b) $B^{(3)}(x|y,z)$ (a dotted curve) and $B_{SA}^{(3)}(x|y,z)\equiv B^{(2)}(x|y)+B^{(2)}(x|z)$ (a solid curve) for $y/l=0.98$ and $z/l=0.0$. If one employs the superposition approximation $g_1(3|1,2)$

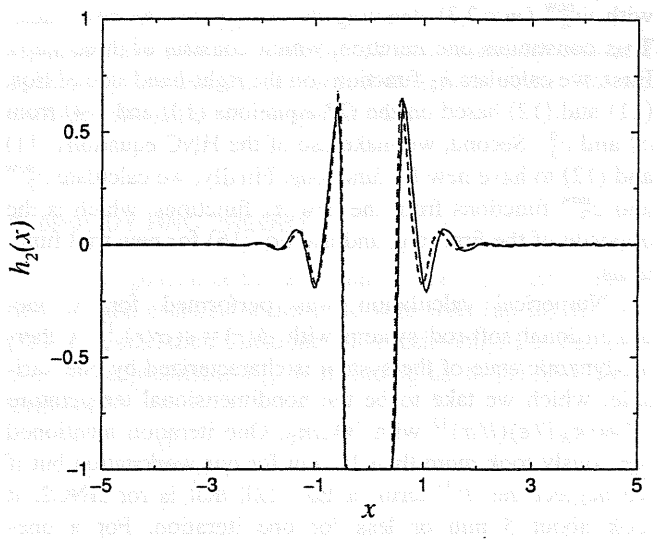

FIG. 1. The two-body correlation function $h_2(x)$ from the two-body HNC theory (a dashed curve) is compared with the experiments ($x>0$, a solid curve) and $M=3$ HNC theory ($x<0$, a solid curve). x is in units of the average interparticle length $l=1/n_0$ with n_0 denoting the density for the one-dimensional system. In all the other figures the interparticle distance is measured this way.

$=g_1(3|1)g_1(3|2)$, we see from Eqs. (11) and (12) that

$$C^{(3)}(x|y,z)=C^{(3)}_{SA}(x|y,z), \tag{17}$$

and a similar equation holds for $B^{(3)}$. We have confirmed numerically that in case three coordinates x, y, and z are not clustered, the above-mentioned relation is satisfied. From Fig. 3 we notice considerable deviation from Eq. (17) when x, y, and z are close to each other forming a cluster.

Summarizing this section, we tried to numerically solve the $M=3$ theory and have shown some results for two- and three-body correlations. In view of the fact that even the HNC2 theory has not been numerically solved heretofore and that our scheme of calculations for $M=3$ theory is not conclusive from the standpoint of convergence, we hope this topic will gather attention and more will be done for numerical as well as analytic investigation.

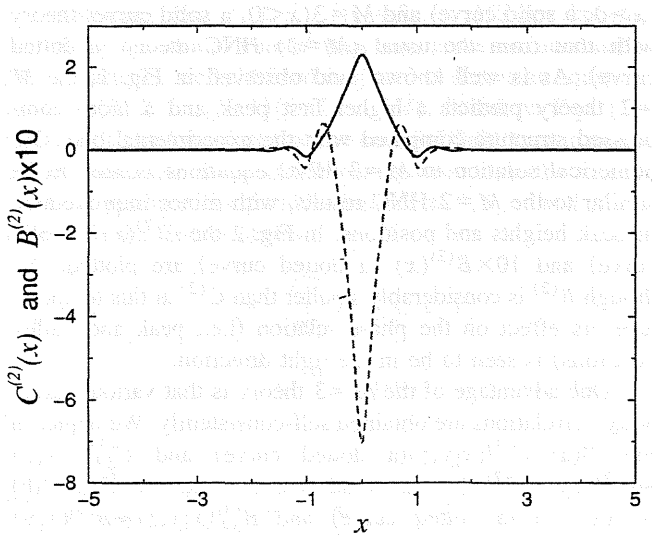

FIG. 2. The $C^{(2)}(x)$ (a solid curve) and $B^{(2)}(x)$ (a dashed curve) from $M=3$ theory. Note that $B^{(2)}(x)$ is multiplied by 10.

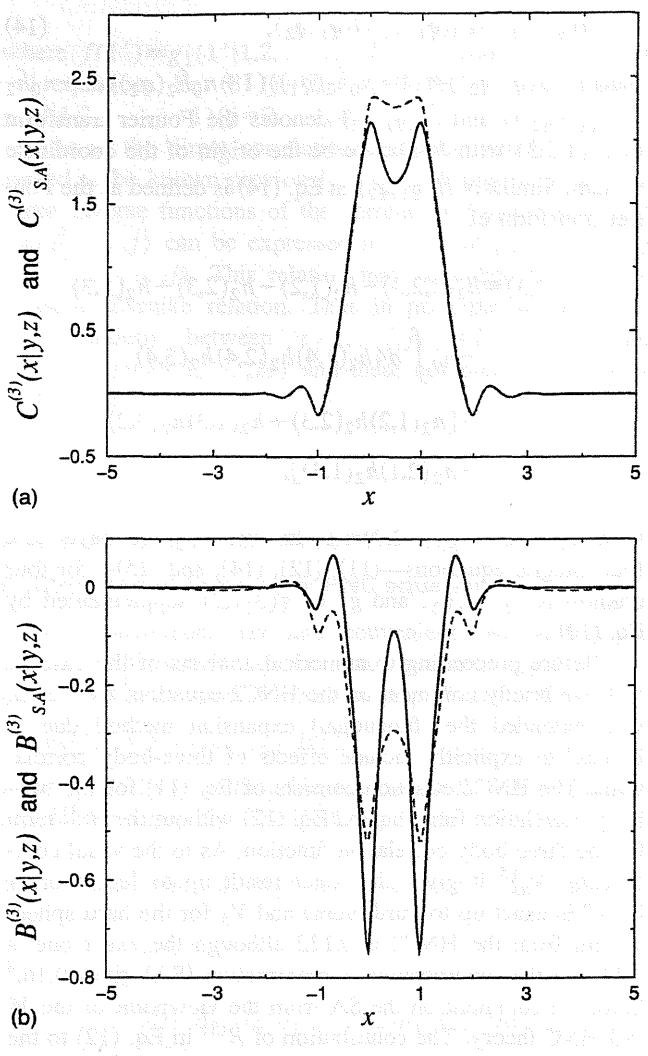

FIG. 3. (a) $C^{(3)}(x|y,z)$ (a dashed curve) from the $M=3$ HNC theory and the superposition approximation $C^{(3)}_{SA}(x|y,z)$ (a solid curve) for $y/l=0.98$ and $z/l=0$. (b) $B^{(3)}(x|y,z)$ (a dashed curve) from the $M=3$ HNC theory and the superposition approximation $B^{(3)}_{SA}(x|y,z)$ (a solid curve) for $y/l=0.98$ and $z/l=0$.

IV. SOME REMARKS

In this paper we developed a theory, which may be called an M-body HNC theory, to study structure of fluids systematically. This is based on the DFT and the non-Markovian expression (7) for higher-order correlation functions. As a first step in this direction we solved the self-consistent equations for the case $M=3$ and compared the results for $h_2(x)$ with experiments and the $M=2$ HNC theory.

The usual ($M=2$) HNC theory consists in neglecting the bridge function $B^{(2)}$ in Eq. (11) entirely. To improve this, a bridge function of a suitable reference system was taken under the assumption that the bridge function has common features shared by simple fluids in general (a RHNC theory[11]). Based on the three-body DFT [$M=3$ in Eq. (9)], a

more systematic approximation Eq. (11) was presented by Percus[6] and also by Verlet.[8] As far as we know, however, Eq. (12), which supplements Eq. (11) and two Ornstein–Zernike relations (13), (14), to give a closed set of equations for $g_2(1,2)$ and $g_3(1,2,3)$, has not been given up to now. In passing it is noted that our theory is not limited to $M=3$. As M becomes large however, numerical solutions for the M-body HNC theory seem to be more and more difficult and it is highly desirable to have some general insights into the solution of the M-body ($M=2,3,\ldots$) HNC theory. This is seen also from the important roles played by the HNC theory to study static structures in liquids[5] and the glass transition.[12]

ACKNOWLEDGMENTS

The author expresses his sincere gratitude to Professor F. Hirata (Institute for Molecular Science, Okazaki) and Professor M. Kinoshita (Kyoto University) for useful discussions and comments. He also thanks J. Yoshiwara (Hitachi Corporation) for help in numerical calculations at an early stage of this study.

[1] For reviews, see A. D. J. Haymet Annu. Rev. Phys. Chem. **38**, 89 (1987); D. W. Oxtoby, in *Liquid, Freezing, and the Glass Transition*, edited by J. P. Hansen, D. Levesque, and J. Zinn-Justin (Elsevier, New York, 1990).
[2] Y. Singh Phys. Rep. **207**, 351 (1991).
[3] D. Chandler, J. D. McCoy, and S. J. Singer, J. Chem. Phys. **85**, 5971 (1986) T. Munakata, S. Yoshida, and F. Hirata, Phys. Rev. E **54**, 3687 (1996).
[4] T. Munakata, Phys. Rev. E **50**, 2347 (1994); T. Takahashi and T. Munakata, *ibid.* **56**, 4344 (1997).
[5] J. P. Hansen and I. R. McDonald, *Theory of Simple Liquids* (Academic, New York, 1986).
[6] J. Percus, in *The Equilibrium Theory of Classical Fluids*, edited by H. L. Frisch and J. L. Lebowitz (Benjamin, New York, 1964).
[7] J. M. J. van Leeuwen, J. Groeneveld, and J. de Boer, Physica (Amsterdam) **25**, 792 (1959); T. Morita and H. Hiroike, Prog. Theor. Phys. **23**, 1003 (1960).
[8] L. Verlet, Physica (Amsterdam) **30**, 95 (1964); **31**, 959 (1965).
[9] C. W. Gardiner, *Handbook of Stochastic Methods* (Springer, Berlin, 1982).
[10] P. J. Flory, *Statistical Mechanics of Chain Molecules* (Interscience, New York, 1969).
[11] F. Lado, Phys. Rev. A **8**, 2548 (1973).
[12] M. Cardenas, S. Franz, and G. Parisi, J. Phys. A **31**, 163 (1998).

Temperature control for simulated annealing

Toyonori Munakata[1] and Yasuyuki Nakamura[2]
[1]*Department of Applied Mathematics and Physics, Kyoto University, Kyoto 606, Japan*
[2]*Department of Informatics, Nagoya University, Nagoya 464, Japan*
(Received 17 January 2001; revised manuscript received 12 June 2001; published 25 September 2001)

The optimal cooling schedule for simulated annealing is formulated to derive a differential equation for the time-dependent temperature $T(t)$. Based on this equation, the long-term behavior of $T(t)$, entropy production, and the Kullback-Leibler entropy are studied. For some simple examples, such as a many-level system and the small scale traveling salesman problem, the explicit time dependence of the temperature is obtained. Some comments are given on simulated annealing based on Tsallis statistics.

DOI: 10.1103/PhysRevE.64.046127 PACS number(s): 05.10.−a, 02.50.Ey, 02.70.Uu

Simulated annealing is a stochastic technique for searching for the (energy) minima of complex discrete or continuous systems [1]. Because of its generality and simplicity, simulated annealing has been applied to various optimization problems, such as the ground-state energy of spin-glass systems and protein folding in condensed-matter physics and the design of integrated circuits and the traveling salesman problem (TSP) in engineering [2]. The key feature of the annealing algorithm is to utilize thermal noise to allow moves that may lead to an increase of the energy and drive the system out of a local minimum. The strength of the noise, which is measured by the time-dependent temperature $T(t)$, is reduced asymptotically to zero, where the system ceases to change and takes usually a local and occasionally the global minimum state.

From both practical and theoretical standpoints, the optimal cooling schedule plays an important role in simulated annealing and there have been some studies on this issue [2–4]. Some related problems, such as the cooling schedule that ensures global optimization [5] and the residual energy as a function of the cooling rate [6], have also gathered considerable interest, reflecting the general popularity of simulated annealing as a tool for optimization. In this paper we derive a differential equation for the temperature $T(t)$ based on optimal control theory [7] and discuss some aspects of simulated annealing based on this equation.

We start from the master equation for the probability $p(\mathbf{x},t)$ of the system to be found in the state $\mathbf{x}$ at time t. Denoting by $W(\mathbf{x}\to\mathbf{x}')$ the transition rate from $\mathbf{x}$ to $\mathbf{x}'$, we have

$$\partial p(\mathbf{x},t)/\partial t=\sum_{\mathbf{x}'} D(\mathbf{x},\mathbf{x}')p(\mathbf{x}',t), \tag{1}$$

where $D(\mathbf{x},\mathbf{x}')=W(\mathbf{x}'\to\mathbf{x})$ for $\mathbf{x}\neq\mathbf{x}'$ and $D(\mathbf{x},\mathbf{x})=-\Sigma_{\mathbf{x}''(\neq\mathbf{x})}W(\mathbf{x}\to\mathbf{x}'')$. It is convenient to express Eq. (1) as

$$d\mathbf{P}(t)/dt=D(t)\mathbf{P}(t), \tag{2}$$

where $\mathbf{P}(t)$ denotes the column vector with elements $p(\mathbf{x},t)$. We will assume the detailed balance condition

$$e^{-E(\mathbf{x})/T(t)}W(\mathbf{x}\to\mathbf{x}')=e^{-E(\mathbf{x}')/T(t)}W(\mathbf{x}'\to\mathbf{x}), \tag{3}$$

where $E(\mathbf{x})$ is the energy (or cost) of the system and the time dependence of $D(t)$ comes from that of the temperature. For later use the equilibrium distribution

$$p_{\mathrm{eq}}(\mathbf{x}|T(t))=\exp[-E(\mathbf{x})/T(t)]/Z_c \tag{4}$$

at temperature $T(t)$ is introduced here.

We try to minimize the expectation value of the energy $\langle E\rangle(\tau)\equiv\Sigma E(\mathbf{x})p(\mathbf{x},\tau)$ at some specified time τ. For the purpose we consider the functional

$$G[\mathbf{P},T,\Lambda]\equiv\int_0^T dt\sum_{\mathbf{x}}\left\{E(\mathbf{x})\sum_{\mathbf{x}'}D(\mathbf{x},\mathbf{x}')p(\mathbf{x}',t)-\Lambda(\mathbf{x},t)\times\left[\partial p(\mathbf{x},t)/\partial t-\sum_{\mathbf{x}'}D(\mathbf{x},\mathbf{x}')p(\mathbf{x}',t)\right]\right\}. \tag{5}$$

The second term with the Lagrange multiplier $\Lambda(\mathbf{x},t)$ represents the constraint that $p(\mathbf{x},t)$ satifies Eq. (1) and the first term is reduced to $\langle E\rangle(\tau)-\langle E\rangle(0)$ which is to be minimized. The variational conditions $\delta G/\delta p(\mathbf{x},t)=0$, $\delta G/\delta T(t)=0$ lead to the following equations:

$$d\mathbf{\Lambda}(t)/dt=-D^T[\mathbf{\Lambda}(t)+\mathbf{E}], \tag{6}$$

$$[\mathbf{E}+\mathbf{\Lambda}(t)]^T[\partial D(t)/\partial T(t)]\mathbf{P}(t)=0, \tag{7}$$

where $\mathbf{\Lambda}(t)$ and $\mathbf{E}$ are the column vectors with elements $\Lambda(\mathbf{x},t)$ and $E(\mathbf{x})$, respectively, and D^T denotes the transpose of D. The condition $\delta G/\delta\Lambda(\mathbf{x},t)=0$ leads to Eq. (1). Equation (6) for the Lagrange multiplier is solved iteratively to be $\mathbf{\Lambda}(t)=-\int_0^t ds\, M^T(s,t)D^T(s)\mathbf{E}$ where we set $\mathbf{\Lambda}(t=0)=\mathbf{0}$ and the matrix $M(s,t)$ is defined by

$$M(s,t)=\sum_{n=0}^{\infty}(-1)^n\int_s^t dt_1\times\int_s^{t_1}dt_2\cdots\int_s^{t_{n-1}}dt_n D(t_n)\cdots D(t_1), \tag{8}$$

which satisfies $M(t,t)=M(s,s)=I$ (a unit matrix) and $\partial M(s,t)/\partial t=-M(s,t)D(t)$ and $\partial M(s,t)/\partial s=D(s)M(s,t)$. Inserting the solution $\mathbf{\Lambda}(t)$ into Eq. (7), we have

$$\mathbf{E}^T(t)[\partial D(t)/\partial T(t)]\mathbf{P}(t)=0, \tag{9}$$

where the time-dependent energy is defined as $\mathbf{E}(t) \equiv M^T(0,t)\mathbf{E}$ or

$$d\mathbf{E}(t)/dt=-D^T(t)\mathbf{E}(t). \tag{10}$$

The time dependence of the temperature $T(t)$ is more explicitly represented by differentiating Eq. (9) with respect to t to finally obtain

$$dT(t)/dt=\mathbf{E}^T(t)[D(t),dD(t)/dT(t)]\mathbf{P}(t)/\{\mathbf{E}^T(t) \times[d^2D(t)/dT^2(t)]\mathbf{P}(t)\}, \tag{11}$$

where $[A,B]\equiv AB-BA$. The closed set of nonlinear equations (2), (10), and (11) is the main result of this paper. It is worthwhile noting that the dynamics described by Eq. (10) is conjugate to that of $\mathbf{P}(t)$, Eq. (2), and it is readily seen that $d\{\mathbf{E}^T(t)\cdot\mathbf{P}(t)\}/dt=0$. The conjugate dynamics Eq. (10) is characterized by its non-negative eigenvalues (if our system is stable). At large time when $p(\mathbf{x}_0,t)\simeq 1$ with $\mathbf{x}_0$ the state of minimum energy, it is expected from the constancy of the inner product $\mathbf{E}^T(t)\cdot\mathbf{P}(t)$ and confirmed numerically that $E(\mathbf{x},t)$ becomes large except at $\mathbf{x}=\mathbf{x}_0$.

As an application of our theory we first consider an N-level system with energy $E_i=\epsilon(i-1)$ $(i=1,2,\ldots,N)$. Transitions are only between neighboring levels and the activation energy to go down (up) is $\Delta(\epsilon+\Delta)$. For $N=2$,

$$W(1\to 2)=\exp[-(\epsilon+\Delta)/T(t)],$$
$$W(2\to 1)=\exp[-\Delta/T(t)]. \tag{12}$$

In this simple model (12) we can calculate the right hand side of Eq. (11) explicitly and, when $T(t)$ becomes small enough so that $T(t)\ll\Delta$, we have

$$dT(t)/dt=\epsilon T(t)^2\exp\{-(\epsilon+\Delta)/T(t)\}/\{\Delta^2 p_2(t) -(\epsilon+\Delta)^2 p_1(t)\exp[-\epsilon/T(t)]\}. \tag{13}$$

If we further assume that annealing is successful, that is, $p_2(t)\simeq\exp[-\epsilon/T(t)]$ and $p_1(t)\simeq 1$, we have

$$dT(t)/dt=-T^2(t)\exp[-\Delta/T(t)]/(\epsilon+2\Delta), \tag{14}$$

which is solved exactly to give

$$T(t)=\Delta/\ln(t/[2+\epsilon/\Delta]). \tag{15}$$

Thus for a two-level system one has to cool the system extremely slowly, in accordance with the classical result [5]. The residual energy, the expectation of the energy at time τ, is simply given by $\langle E\rangle(\tau)=\epsilon p_2(\tau)=\epsilon[\tau/(2+\epsilon/\Delta)]^{-\epsilon/\Delta} \propto\tau^{-\epsilon/\Delta}$. This power law was derived heuristically before [6].

In view of the important role played by Tsallis statistics in optimization and simulated annealing [8], we study how the slow decay of temperature $T(t)$ is modified if one employs Tsallis instead of Gibbs statistics. According to Tsallis statistics [9], the equilibrium distribution is given by

$$p_{\rm eq}(\mathbf{x}:T)=c/[1+(q-1)E(\mathbf{x})/T]^{1/(q-1)}, \tag{16}$$

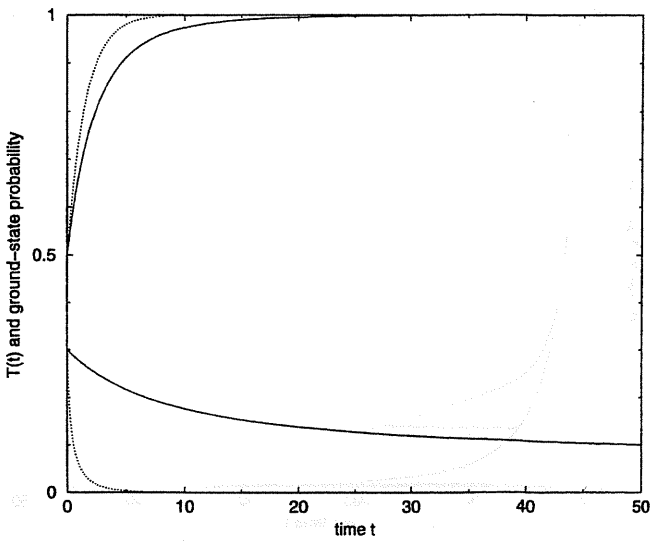

FIG. 1. Temperature $T(t)$ and $p_1(t)$, the probability to be in the ground state 1, for the Gibbs (full curves) and Tsallis (dotted curves) statistics. $T(0)=0.3$, $p_1(0)=0.5$ and $\Delta=0.25$, $\epsilon=1.0$.

with c a normalization constant. We consider the two-level system as before. To satisfy the detailed balance condition, we tentatively consider an additional level 3 with energy $E=\epsilon+\Delta$ and choose the following transition rate:

$$W(1\to 2)=p_{\rm pq}(3)/p_{\rm eq}(1)=1/[1+(q-1)(\epsilon+\Delta)/T]^{1/(q-1)}, \tag{17}$$

$$W(2\to 1)=p_{\rm eq}(3)/p_{\rm eq}(2)=\{[1+(q-1)\epsilon/T]/[1+(q-1) \times(\epsilon+\Delta)/T]\}^{1/(q-1)}. \tag{18}$$

If we take the limit $q\to 1$ we recover the Gibbsian result Eq. (12). The right hand side of Eq. (11) is calculated easily as in the Gibbsian case and after lengthy calculations we have, corresponding to Eq. (14),

$$dT(t)/dt=-\alpha T(t), \tag{19}$$

with $\alpha=[\epsilon/(\epsilon+\Delta)]^{1/(q-1)}(q-1)/(2-q)$. Thus for $1<q<2$ we have an exponential decay of the optimal temperature. This rapid decay of $T(t)$, compared with the logarithmic decay in the Gibbsian case, can be profitably used in simulated annealing [8]. In Fig. 1 we show the optimal $T(t)$ and the ground-state probability $p_1(t)$ for the Gibbsian case (12) and the Tsallis case (17) and (18). The temperature variation is found to precisely follow the theoretical predictions (15) and (19) for large time $t\gg 1$.

Here we note that the exponential asymptotic cooling (19) is different from the well-known power law asymptotic cooling for generalized simulated annealing [8(a)] and we briefly touch upon this point. In Ref. [10] it is shown that the generalized simulated annealing with power law cooling [8(a)] satisfies the (weak) ergodicity property. That is, the final state arrived at by the simulated annealing is independent of the initial distribution function. On the other hand, in our paper we do not claim that we give a sufficient or ergodicity condition for successful simulated annealing. Instead, we

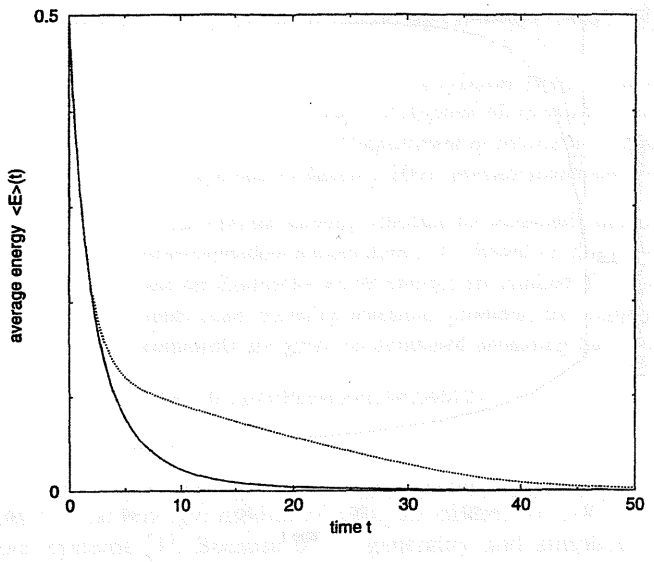

FIG. 2. Average energy $\langle E\rangle(t)$ from the optimal temperature $T(t)$ (full curve) and from the linear temperature $T_L(t)=T(0)-at$ (dotted curve) for a two-level system ($\Delta=0.25$, $\epsilon=1.0$).

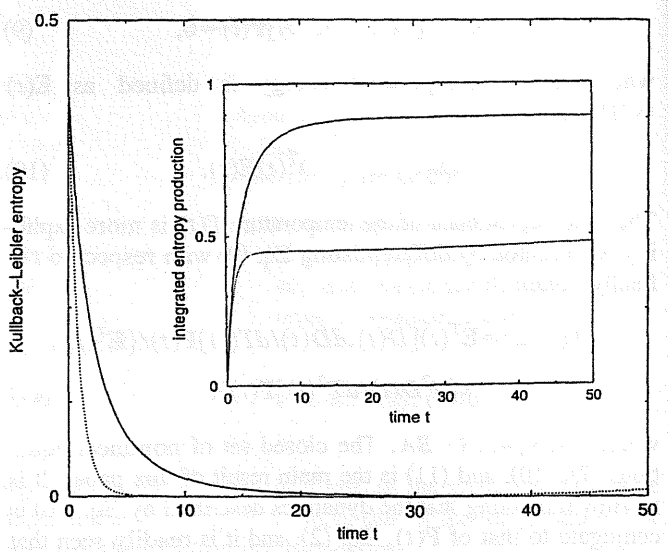

FIG. 3. Kullback-Leibler entropy $S_{\mathrm{KL}}(t)$ from the optimal $T(t)$ (full curve) and from the linear variation $T_L(t)=T(0)-at$ (dotted curve). Inset: Integrated entropy production $\int_0^t dt'\,\sigma(t')$ from the optimal $T(t)$ (full curve) and from the linear variation $T_L(t)=T(0)-at$ (dotted curve). The system and the initial conditions are the same as those in Fig. 2.

show that, if the initial distribution and other conditions for the system parameters happen to be properly chosen, and consequently if the calculation is successful in the sense that $T(t)$ becomes very small for large t, then the temperature variation should be inverse logarithmic and exponential for Gibbsian and generalized simulated annealing, respectively. In this sense the exponential behavior of $T(t)$ [Eq. (9)] is not contradictory with the power law [8(a),10].

We give here two comments: one is on how $\langle E\rangle(t)$ depends on the temperature variation and the other on how the optimal $T(t)$ changes as N increases from 2. For the two-level system considered above $\langle E\rangle(t)$ obtained from the optimal $T(t)$ and from the linear variation $T_L(t)=T(0)-at$, with $T(0)=0.5$ and a determined from $T_L(\tau=50)=T(\tau=50)$, are compared in Fig. 2. Here we took $p_1(0)=0.5$ for both cases. We note that the optimal $T(t)$ depends only on the initial probability distribution $p(\mathbf{x},t=0)$ and temperature $T(0)$, and it is reasonable that $\langle E\rangle(t)$ from the optimal $T(t)$ is always smaller than that from the linear one. For an N-level system (up to $N\simeq 10^3$), we found that the optimal $T(t)$ behaves nearly the same as in the two-level system for long times $t>50$. However, in the range $0<t<50$ cooling becomes slower as N becomes larger. A more complicated many-level system, a small scale TSP, will be touched upon later.

Next we consider the entropy production $\sigma(t)$ and the Kullback-Leibler entropy $S_{\mathrm{KL}}(t)$ in the process of simulated annealing. Introducing the statistical entropy $S_{\mathrm{st}}(T)$ by $S\equiv-\Sigma p(\mathbf{x},t)\ln p(\mathbf{x},t)$, we know that the entropy production $\sigma(t)dt$ in time dt, defined below, is non-negative [11]:

$$dS_{\mathrm{st}}(t)=d\langle E\rangle(t)/T(t)+\sigma(t)dt. \tag{20}$$

The Kullback-Leibler entropy $S_{\mathrm{KL}}(t)$ [12], which is also non-negative, is defined here as a measure of the distance between the actual distribution $p(\mathbf{x},t)$ and the equilibrium distribution at temperature $T(t)$, Eq. (4),

$$S_{\mathrm{KL}}(t)=\Sigma p(\mathbf{x},t)\ln[p(\mathbf{x},t)/p_{\mathrm{eq}}(\mathbf{x}:T(t))]. \tag{21}$$

$\sigma(t)$ and $S_{\mathrm{KL}}(t)$ are related to each other through

$$S_{\mathrm{KL}}(t)-S_{\mathrm{KL}}(0)=-\int_0^t dt'\sigma(t')-\int_0^t \delta\langle E\rangle \times(t')\frac{dT(t')}{dt'}\Big/T^2(t'), \tag{22}$$

where $\delta\langle E\rangle(t)\equiv\langle E\rangle(t)-\langle E\rangle_{\mathrm{eq}}(t)$ with $\langle E\rangle_{\mathrm{eq}}(t)\equiv\Sigma E(\mathbf{x})p_{\mathrm{eq}}(\mathbf{x}:T(t))$. Since it is expected that $dT(t)/dt<0$ and $\delta\langle E\rangle(t)>0$ in a general annealing process, we see that the first and the second terms of Eq. (22) are negative and positive, respectively. In simulated annealing, it is desirable that the actual distribution $p(\mathbf{x},t)$ precisely follows the equilibrium distribution (4) and in this sense the optimal annealing process represented by Eq. (11) is expected to keep $S_{\mathrm{KL}}(t)$ small. We note that if $p(\mathbf{x},t)\simeq p_{\mathrm{eq}}(\mathbf{x}:T(t))$ for any t, it is proved that $\sigma(t)=0$ and also $\delta\langle E\rangle(t)=0$; thus $dS_{\mathrm{KL}}(t)/dt=0$ (as it should). However, in actual simulated annealing the cooling rate $|dT(t)/dt|$ cannot be zero and the system has to go through an irreversible process in which $\sigma(t)>0$. The question we would like to address is how $S_{\mathrm{KL}}(t)$ is kept small, whether the degree of irreversibility represented by $\sigma(t)$ is made small or the positivity of $\sigma(t)$ is used in order to counteract the second term of Eq. (22). We compare in Fig. 3 $S_{\mathrm{KL}}(t)$ for the two temperature variations represented in Fig. 2. Also shown (inset) is the integrated entropy production $\int_0^t\sigma(t')dt'$, from which we notice that entropy production $\sigma(t)$ is larger for optimal control. For $t<20$, $S_{\mathrm{KL}}(t)$ is definitely larger for the optimal case than the linear case. However, the linear $S_{\mathrm{KL}}(t)$ begins to increase

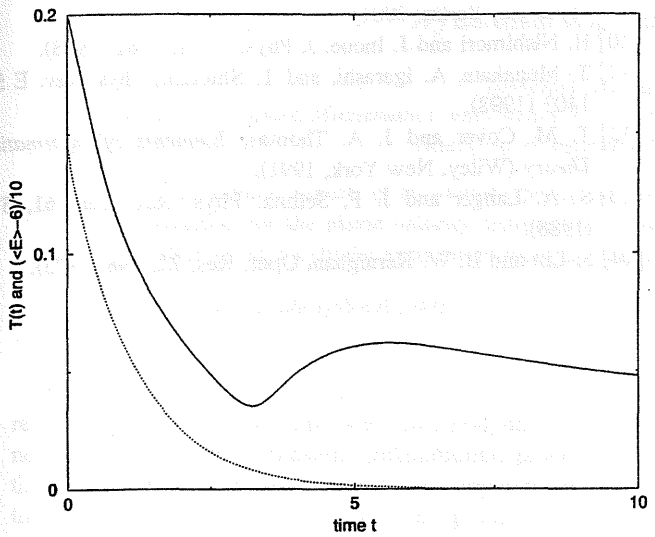

FIG. 4. $T(t)$ (full curve) and $\langle E\rangle(t)$ (dotted curve) for the TSP with $M=6$ cities. Note that actually $[\langle E\rangle(t)-E_{\min}]/10$ is plotted instead of $\langle E\rangle(t)$.

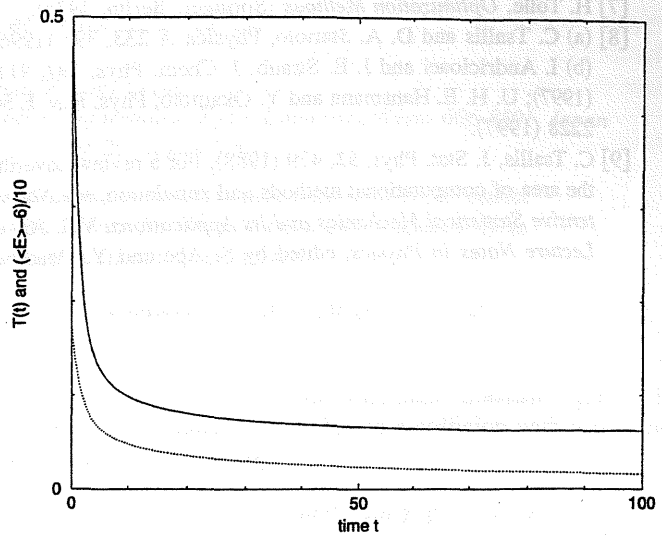

FIG. 5. The same as Fig. 4 except that the activation energy $\Delta=0.3$ is introduced and the initial temperature $T(0)$ is slightly higher.

around $t\simeq 30$, signaling that the function $p(\mathbf{x},t)$ deviates from the equilibrium one, Eq. (4). In passing it is noted that for the N-level model this increase of $S_{\mathrm{KL}}(t)$ seems to be a general tendency for cooling schemes other than the optimal one.

Up to now we have been mainly concerned with a rather simple N (=2) -level system, which underlies many complex systems [13]. In order to make contact with Monte Carlo simulations, we apply the optimal cooling schedule to a small scale TSP with $M=6$ cities put at (0, $\pm$0.5), (1, $\pm$0.5), and (2, $\pm$0.5) with the minimum path length $E_{\min}=6$. For the neighborhood structure of the paths we employ the Lin-Kernighan [14] 2-opt transition. Then $\frac{1}{6}$ of the elements of the transition matrix W or $D(t)$ in Eq. (2), which is an $N\times N$ matrix with $N=(M-1)!/2=60$, turn out to be nonzero. In Fig. 4 we plot the optimal $T(t)$ and the average energy obtained from the initial condition $T(0)=0.2$ and $p(i,t=0)\propto\exp[-E_i/T(0)]$. The energy (=path length) is seen to be rapidly approaching $E_{\min}$, although $T(t)$ has a bump around $t=5$. In this case we imposed no activation energy in the transition to states with lower energy (i.e., we used the Metropolis algorithm) in contrast to the N-level system studied before. If we increase the initial temperature $T(0)$, we cannot get a *physical* solution, because the initial (equilibrium) distribution becomes more diffuse and goes out of the basin of the desirable attractor of Eqs. (2), (10), and (11). To cope with this situation we introduced the activation energy $\Delta=0.3$ in the transition to states with lower energy. The result is shown in Fig. 5 for $T(0)=0.5$, where $T(t)$ and also $\langle E\rangle(t)$ change more slowly compared with Fig. 4 but are attracted to the desirable stationary state of the coupled equations (2), (10), and (11). Thus introducing a nonzero Δ seems to extend the basin of the physical attractor with inevitable slow cooling. Here we comment on the utility of our approach in connection with realistic optimization problems. Usually, simulated annealing for optimization problems involves many parameters, the values of which we can choose to achieve good performance. Before embarking on simulated annealing for the large scale problem at hand, one can guess desirable ranges of each parameter by solving the differential equation (11) for a small scale problem, as we did for the case of the TSP.

In this paper we studied temperature control for simulated annealing and derived a first order differential equation (11) supplemented by Eqs. (2) and (10), whose properties were studied for some simple model systems such as an N-level system and a small scale TSP. Our concern here was directed to conceptual rather than practical aspects of the simulated annealing methods. It is hoped that further studies of the set of equations (11), (2), and (10) will shed more light on technical aspects of simulated annealing.

One of the authors (T.M.) expresses his gratitude to S. Ikemoto for useful discussions at an early stage of this study.

[1] S. Kirkpatrick, C. D. Gelatt, and M. P. Vecchi, Science **220**, 671 (1983).
[2] P. van Laarhoven and E. H. L. Aarts, *Simulated Annealing: Theory and Applications* (Kluwer, Dordrecht, 1992).
[3] K. H. Hoffmann and P. Salamon, J. Phys. A **23**, 3511 (1990).
[4] T. M. Heskes, E. T. P. Slijpen, and B. Kappen, Phys. Rev. E **47**, 4457 (1993).
[5] S. Geman and D. Geman, IEEE Trans. Pattern Anal. Mach. Intell. **6**, 721 (1984).
[6] D. A. Huse and D. S. Fisher, Phys. Rev. Lett. **57**, 2203 (1986); Y. Kabashima and S. Shinomoto, J. Phys. Soc. Jpn. **60**, 3993 (1991).

[7] H. Tolle, *Optimization Methods* (Springer, Berlin, 1975).
[8] (a) C. Tsallis and D. A. Stariolo, Physica A **233**, 395 (1996); (b) I. Andricioaei and J. E. Straub, J. Chem. Phys. **107**, 9117 (1997); U. H. E. Hansmann and Y. Okamoto, Phys. Rev. E **56**, 2228 (1997).
[9] C. Tsallis, J. Stat. Phys. **52**, 479 (1988). For a review covering the area of computational methods and simulation, see *Nonextensive Statistical Mechanics and Its Applications*, Vol. 560 of *Lecture Notes in Physics*, edited by S. Abe and Y. Okamoto (Springer, Berlin, 2001).
[10] H. Nishimori and J. Inoue, J. Phys. A **31**, 5661 (1998).
[11] T. Munakata, A. Igarashi, and T. Shiotani, Phys. Rev. E **57**, 1403 (1998).
[12] T. M. Cover and J. A. Thomas, *Elements of Information Theory* (Wiley, New York, 1991).
[13] S. A. Langer and J. P. Sethna, Phys. Rev. Lett. **61**, 570 (1988).
[14] S. Lin and B. W. Kernighan, Oper. Res. **21**, 498 (1973).

Dynamical aspects of an adiabatic piston

Toyonori Munakata and Hideki Ogawa
Department of Applied Mathematics and Physics, Graduate School of Informatics, Kyoto University, Kyoto 606-8501, Japan
(Received 23 February 2001; published 29 August 2001)

Dynamical aspects of an adiabatic piston are investigated, based on the mass ratio expansion of the master equation for the piston velocity distribution function. Simple theory for piston motion and relaxation of an ideal gas in a cylinder turns out to reproduce our numerical experiments quantitatively.

DOI: 10.1103/PhysRevE.64.036119 PACS number(s): 02.50.−r, 05.40.−a, 05.20.−y

The adiabatic piston has gathered considerable attention recently, partly in connection with thermodynamics and kinetics [1,2] to predict transient (relaxational) processes and the final equilibrium state and partly its apparent relation to the ratchet dynamics [3]. In short the problem is how an *adiabatic* piston, which separates a gas-filled cylinder into two parts with different pressure and/or temperature, moves and how the whole system relaxes towards its equilibrium state. Since we are interested in dynamics of the whole piston-gas system, we study the problem based mainly on the master equation [4] for the piston velocity distribution function $p(V,t)$ and also on thermodynamic considerations to deal with relaxation processes in the piston-gas system.

Our system consists of a cylinder with length L and a piston with mass M, which separates the cylinder into the left and right parts ($i=l,r$), each containing $N_i(i=l,r)$ ideal gas particles with mass m. The density $n_i(i=l,r)$ is given by

$$n_l=N_l/(XA), \quad n_r=N_r/[(L-X)A], \tag{1}$$

where X is the length of the left cell and A denotes the cross sectional area of the cylinder. To derive a master equation for the piston velocity distribution function $p(V,t)$, let us consider the collision between the piston with velocity V and a particle with velocity v in the left cell. From the conservation of energy and momentum, the velocity after the collision V' of the piston is

$$V'=V+2m(v-V)\Theta(v-V)/(M+m), \tag{2}$$

where the step function [$\Theta(x)=1(0)$ for $x>0(x<0)$] shows that the collision is possible only for the case $v>V$. Assuming that the velocity distribution of the ideal gas in the left cell is Maxwellian with temperature T_l, the transition rate $W_l(V\to V')$ of the piston velocity from V to V' is given by

$$W_l(V\to V')=n_l[(M+m)/(2m)]^2(V'-V)Af_M \times([\{M+m\}V'-\{M-m\}V]/\{2m\};T_l) \times\Theta(V'-V) \tag{3}$$

with

$$f_M(v;T)=(2\pi T/m)^{-1/2}\exp[-mv^2/(2T)]. \tag{4}$$

Here and hereafter we set the Boltzmann constant equal to 1. Similarly the transition rate due to a collision with a particle in the cell r is given by

$$W_r(V\to V')=n_r[(M+m)^2/(2m)^2](V-V')Af_M \times([\{M+m\}V'-\{M-m\}V]/\{2m\};T_r) \times\Theta(V-V'). \tag{5}$$

Since the piston velocity V changes due to collisions with particles in both the right and left cells, the (total) transition rate $W(V\to V')$ is defined by $W(V\to V')\equiv W_l(V\to V')+W_r(V\to V')$, and we obtain the following master equation for the probability density $p(V,t)$ of the piston velocity:

$$\partial p(V,t)/\partial t=\int dV'[W(V'\to V)p(V',t) - W(V\to V')p(V,t)]. \tag{6}$$

Now we apply the mass ratio expansion [4,5] method developed by van Kampen to transform the complicated integrodifferential equation (6) to a tractable Fokker-Planck equation. Referring the details of the derivation to the original paper [5], we only give an essential idea behind the mass ratio expansion. Introducing the smallness parameter ϵ by

$$\epsilon\equiv m/(m+M), \tag{7}$$

we express velocity of the piston V as the sum of its deterministic part V_D and fluctuation $\epsilon^{1/2}u$ as

$$V=V_D+\epsilon^{1/2}u. \tag{8}$$

Next from Eqs. (2), (3), and (5), we notice that the transition rate $W(V\to V')$ can be expressed as $\epsilon^{-1}\tilde{W}(V;[V'-V]/\epsilon)$ with $\tilde{W}(V,a)\equiv(Aa/4)[n_lf_M(\{V+a/2\};T_l)\Theta(a)-n_rf_M(\{V+a/2\};T_r)\Theta(-a)]$ and this allows immediately a formal Taylor expansion of the master equation (6) [5]. For V_D we have the following evolution equation:

$$dV_D(t)/dt=\epsilon\alpha_1(V_D:T_l,T_r,X), \tag{9}$$

where the nth jump moment $\alpha_n(n=1,2,\ldots)$ is defined as

$$\alpha_n(V:T_l,T_r,X)=\int daa^{n+1}A[n_lf_M(V+a/2:T_l)\Theta(a) - n_rf_M(V+a/2:T_r)\Theta(-a)]/4. \tag{10}$$

The X dependence of α_n comes from the X dependence of the density, see Eq. (1). For the fluctuation u in Eq. (8) we have the Fokker-Planck equation

$$\partial p(u,t)/\partial t = -\epsilon^{1/2}\partial/\partial u[\{\alpha_1(V_D+\epsilon^{1/2}u)-\alpha_1(V_D)\}p] + \sum_{n=2}\{\epsilon^{n/2}/(n!)\}(-\partial/\partial u)^n[\alpha_n(V_D+\epsilon^{1/2}u)p]. \tag{11}$$

Dynamics of $X(t)$ is naturally described by $dX/dt = V_D + \epsilon^{1/2}u$. We employ a simplifying approximation in which the stochastic variable X is replaced by its average over the distribution function $p(u,t)$, that is,

$$dX/dt = V_D + \epsilon^{1/2}\langle u(t)\rangle. \tag{12}$$

The method of mass ratio expansion has been mainly used for the case $T_l = T_r$ to study relaxation of the piston velocity to its Maxwellian equilibrium distribution [5]. We will use it to study the relaxation of the whole system (piston and gas) towards the equilibrium state.

From Eqs. (9) and (11) we see that the dynamics is determined by α_n, Eq. (10). Although it is not difficult to calculate these coefficients numerically, we calculate some lowest order coefficients analytically for later convenience. Omitting T and X dependences we have

$$\alpha_n(V) = B_l\int_0^\infty daa^{n+1}\exp[m(a+2V)^2/(8T_l)] - B_r\int_{-\infty}^0 daa^{n+1}\exp[m(a+2V)^2/(8T_r)], \tag{13}$$

where

$$B_i = An_i(m/2\pi T_i)^{1/2}/4 \quad (i=l,r). \tag{14}$$

From this we find, after some calculation, that

$$\alpha_1(V=0) = A(n_lT_l - n_rT_r)/m = A(p_l-p_r)/m, \tag{15}$$

$$\alpha_2(V=0) = 8A(2\pi)^{-1/2}[n_l(T_l/m)^{3/2}+n_r(T_r/m)^{3/2}] \equiv D_0(>0), \tag{16}$$

where the equation of state for the ideal gas as used in Eq. (15) is

$$p_i = n_iT_i(i=l,r). \tag{17}$$

As for the derivatives of $\alpha_n(V)$ with respect to V similar calculations yield

$$\alpha_1'(V=0) = -4A[n_lT_l^{1/2}+n_rT_r^{1/2}]/(2\pi m)^{1/2} \equiv -\zeta(<0), \tag{18}$$

$$\alpha_2'(V=0) = 6A[-p_1+p_2]/m, \tag{19}$$

$$\alpha_1''(V=0) = 2A[p_l/T_l - p_r/T_r] \equiv \sigma, \tag{20}$$

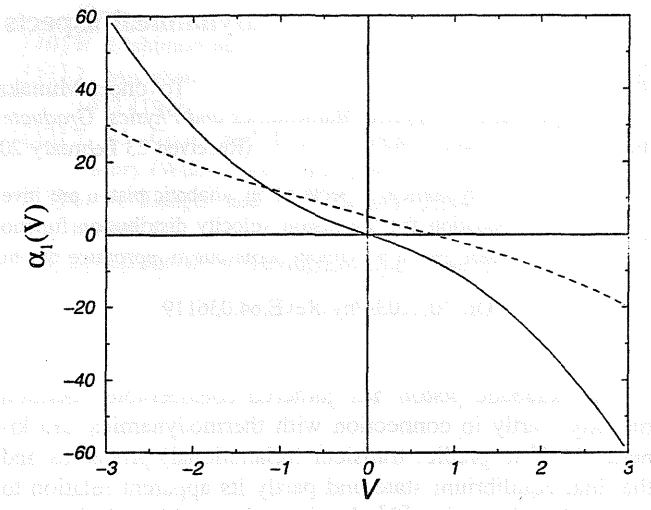

FIG. 1. Driving force $\alpha_1(V)$ for the cases $p_l > p_r$ (dotted curve, $T_l=3, n_l=2, T_r=1, n_r=1$) and $p_l=p_r$ (full curve, $T_l=3, n_l=1, T_r=1, n_r=3$). The full curve goes through the point (0,0) since $\alpha_1(0)=0$. It is noted that all the physical quantities to appear in this and subsequent figures are nondimensional, with units m (the mass of an ideal gas perticle), the Boltzmann constant and A (the cross sectional area of the cylinder).

$$\alpha_1'''(V=0) = -4A[n_l/\sqrt{T_l}+n_r/\sqrt{T_r}](m/2\pi)^{1/2} \equiv -\mu^2(<0). \tag{21}$$

Furthermore we note that $\alpha_2''(V=0) = 12\sqrt{2}A(m\pi)^{-1/2}[p_1/\sqrt{T_1}+p_2/\sqrt{T_2}]$ is a positive quantity. σ defined by Eq. (20) may be considered to be symmetry breaking in the sense that even if the mechanical force balances, i.e., $p_l=p_r$, σ does not necessarily vanish and can give rise to directional (toward the region of higher temperature) piston motion as shown below.

First we consider an infinite system $N_l, N_r = \infty$. In this case piston movement does not affect the thermodynamic conditions such as temperature and pressure and the problem is to obtain the stationary piston velocity. Hereafter in our numerical presentation we put $m=1$ and $A=1$ and all the quantities are nondimensional. In Fig. 1 we plot $\alpha_1(V)$ for the case $p_l=6(T_l=3, n_l=2)$, and $p_r=1(T_r=1, n_r=1)$ (dotted curve). The force on the piston due to the unbalance of the pressure p_l and p_r is represented by the ordinate of the point [see Eq. (15)] where the curve crosses the y axis and the stationary velocity V_D is given by the abscissa of the point where the curve crosses the x axis in Fig. 1. The physical origin of V_D becomes clear if we explicitly write down (to order $\epsilon^{3/2}$) the equation of motion (9) from Eqs. (15) and (18),

$$(M+m)dV_D/dt = A(p_l-p_r) - m\zeta V_D. \tag{22}$$

Thus the stationary (or terminal) velocity V_D is determined by the balance of the driving force and the frictional force. When $p_l=p_r$ the macroscopic velocity vanishes, $V_D=0$ (see Fig. 1 full curve) since $\alpha_1(V=0)=0$. In this situation, dynamics should be discussed based on Eq. (11). Taking the

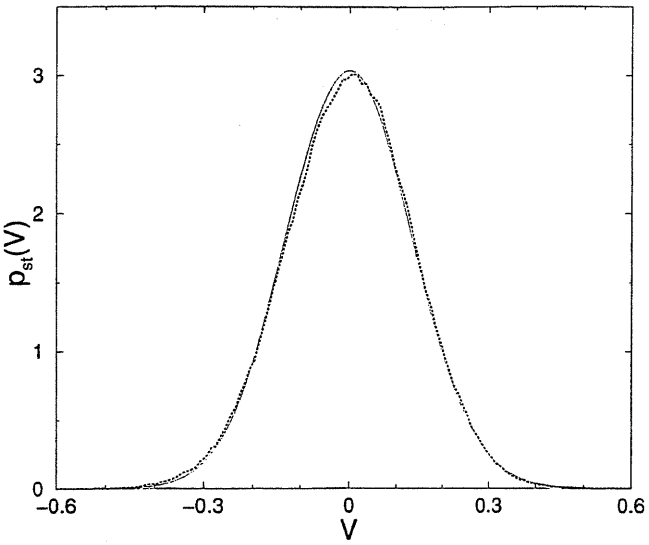

FIG. 2. Stationary distribution of the piston velocity for an infinite system from experiments (dotted curve) and theory (full curve).

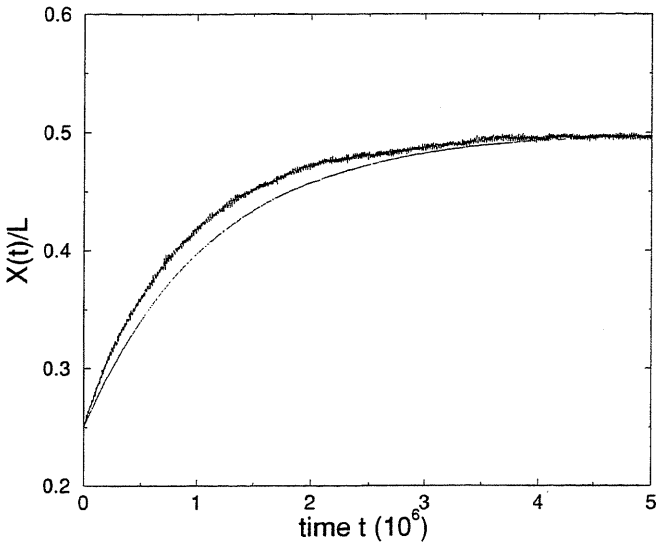

FIG. 3. Piston position $X(t)$ relaxing toward $X(t=\infty)=L/2$. The curve with jags is the result of averages over 50 experiments and the full curve is from theory.

dominant terms into consideration, we reduce Eq. (11) to the following Fokker-Planck equation

$$\partial p(u,t)/\partial t = -\partial/\partial u[-\{d\Phi(u)/du\}p] + \epsilon(D_0/2)(\partial/\partial u)^2 p, \tag{23}$$

where we have defined the effective potential by

$$\Phi(u) = \epsilon\zeta u^2/2 - (\sigma/6)\epsilon^{3/2}u^3 + \epsilon^2\mu^2 u^4/24. \tag{24}$$

Since thermodynamic parameters do not change in time for an infinite system we have a stationary distribution $p_{st}(u)$ from Eq. (23)

$$p_{st}(u) \propto \exp[-\Phi(u)/(\epsilon D_0/2)]. \tag{25}$$

When $T_l \neq T_r$, the symmetry breaking parameter σ does not vanish and the average $\langle u \rangle$ calculated by the distribution function (25) is not zero. More explicitly we can calculate perturbationally the average velocity to obtain [2]

$$\sqrt{\epsilon}\langle u \rangle = \epsilon\sigma D_0/(4\zeta^2) = \sqrt{(\pi/8m)}[\sqrt{T_r} - \sqrt{T_l}]\epsilon. \tag{26}$$

Equation (26) shows that the piston moves in the direction of a hotter region in agreement with numerical experiments for a hard rod system [6] and an ideal gas as shown below.

Now we turn to a system with finite size, where piston movement results in variation of various thermodynamic parameters and the problem is to determine the piston position $X(t)$ as a function of time. For this purpose we examine the time evolution of the system with the main concern put on the piston motion $dX(t)/dt$. Since the piston is heavy and moves slowly we can regard the two cells to be homogeneous, characterized by $T_i(t)(i=l,r)$ and $n_i(t)(i=l,r)$ and we have the equation of motion for the piston from Eq. (26)

$$dX(t)/dt = \sqrt{(\pi/8m)}[\sqrt{T_r} - \sqrt{T_l}]\epsilon. \tag{27}$$

Since the piston energy in the conservation law

$$(N_l/2)dT_l/dt + (N_r/2)T_r/dt + d[M\langle u^2 \rangle/2]/dt = 0$$

is negligible from Eq. (25) and under the condition $N_i(i=l,r) \gg 1$, we have

$$N_l dT_l/dt + N_r dT_r/dt = 0. \tag{28}$$

Finally assuming that mechanical balance $p_l = p_r$ holds, we have

$$N_l T_l/X = N_r T_r/(L-X). \tag{29}$$

From Eqs. (27), (28), and (29) it follows that

$$dX/dt = -\sqrt{(\pi K_0/8mL)}[\sqrt{X} - \sqrt{(L-X)/c}]\epsilon, \tag{30}$$

where $c \equiv N_r/N_l$ and $K_0 \equiv T_l + cT_r$. Instead of showing the rather complicated analytic solution to Eq. (30), we consider the dynamics at the late stage when $X(t)$ approaches the equilibrium point $L/(1+c)$ and we easily obtain simple exponential behavior $\exp(-t/\tau)$ of $X(t)$ with the relaxation time τ given by

$$\tau = (4Lc/\epsilon)\sqrt{2m/\pi K_0(1+c)^3}. \tag{31}$$

Simple exponential behavior, which was first observed in [6], is quantitatively verified below.

Finally in this theoretical part, we consider the thermodynamics of the system. First, from Eqs. (28) and (29) it is seen that the pressure Eq. (17) is a constant, which is in accord with our experimental observation (except for fluctuations). Since the entropy of a one-dimensional ideal gas is given by $S = N \ln[\sqrt{T}/n]$ to an additive constant, we have

$$d(S_l + S_r)/dt = (3/2)N_l[T_l^{-1}dT_l/dt + cT_r^{-1}dT_r/dt], \tag{32}$$

which is rewritten from Eq. (28) as

$$d(S_l+S_r)/dt=(3/2)N_l[T_l^{-1}-T_r^{-1}]dT_l/dt. \quad (33)$$

From the second law we know that the right hand side is non-negative and heat is confirmed to flow from a high to a low temperature region. The same equation is derived if we apply the second law to, e.g., the left cell and study $dS_l \geqslant dQ/T_r=(dE_l+pSdX)/T_r$.

Numerical experiments are rather simple for a system with finite size and a minor modification of a molecular dynamics method for a hard rod system [7] is enough, since we only need to consider elastic collisions of particles with a piston and a wall. In experiments for an infinite system, we take a Monte Carlo (MC) approach. First we choose a time increment Δ and calculate $z_l \equiv \Delta \int dV' W_l(V \to V')$ and $z_r \equiv \Delta \int dV' W_r(V \to V')$ [see Eqs. (3) and (5)]. z_l, and z_r denote the probabilities of the piston with velocity V to collide with the left cell and right cell particles, respectively and $1-z_l-z_r$ is the probability of no collision. In order to avoid more than one collision in time Δ we choose Δ small enough so that $z_l+z_r<0.03$. If a collision with say, the left cell particle occurs, the new velocity V' is chosen according to the probability $W_l(V \to V')/\int dV'' W_l(V \to V'')$. In Fig. 2 we plot the stationary velocity distribution $p_{st}(V)$ (dotted curve), which is based on 8×10^6 MC steps for an infinite system together with the theoretical one(full curve) ($\epsilon=0.01$) for $T_l=1, n_l=0.1, T_r=3$, and $n_r=1/30$. The average velocity is 0.0059 from numerical experiments and 0.0046 from theory. It is noted that not only the mass ratio ϵ but the difference in the thermodynamic parameters of the two cells have effects on the validity of the theoretical prediction for $p_{st}(V)$. Generally the smaller the ϵ and the differences in the thermodynamic parameters, the discrepancy in the stationary velocity distribution function between experiments and theory becomes small. For example, when T_l and T_r differ considerably, fluctuation in pressure becomes large and we have to take fluctuation effects into account. For the finite system we arbitrarily set $N_l=N_r=500(c=1)$, and $L=20\,000$. Experimental piston positions (jagged curve), which are averages over 50 experiments, and theoretical ones (smooth full curve) $X(t)$ are plotted in Fig. 3. The initial condition is $X(0)/L=0.25$, $T_l(0)=1$, and $T_r=3$. If we use Eq. (31) we have $\tau=1.1\times10^6$ and the best fit to experiments is achieved by a single exponential with $\tau=0.94\times10^6$.

Note added in proof. In the molecular dynamics simulation for a system with finite size, the velocity distribution of particles in an ideal gas is not necessarily Maxwellian and this seems to be one of the reasons for the discrepancies between our theory and experiments.

In this paper we studied the adiabatic piston problem based on the mass ratio expansion method. In spite of our neglection of some fluctuation and inhomogeneity effects, our theory turns out to reproduce the experimental results quantitatively. Equations (33) and (31) show that energy flows through the piston so long as the mass of the piston is finite. Thus from our treatment presented above we may say that the piston treated in this paper had better be called the Brownian piston.

[1] J. Piasecki and Ch. Gruber, Physica A **265**, 463 (1999).
[2] Ch. Gruber and J. Piasecki, Physica A **268**, 412 (1999).
[3] F. Juelicher, A. Ajdari, and J. Prost, Rev. Mod. Phys. **69**, 1269 (1997); R. D. Astumian, Science **276**, 917 (1997).
[4] C. W. Gardiner, *Handbook of Stochastic Methods* (Springer, Berlin, 1983).
[5] N. G. van Kampen, Can. J. Phys. **39**, 551 (1961).
[6] E. Kestemont, C. van den Broeck, and M. M. Mansour, Europhys. Lett. **49**, 143 (2000).
[7] M. P. Allen and D. J. Tildsley, *Computer Simulations of Liquids* (Clarendon Press, Oxford, 1987).

過冷却液体の構造
– Molecular dynamicsとDFT –

京都大学大学院情報学研究科*　　宗像 豊哲†　金 鋼‡

概 要

Molecular dynamics と DFT はガラス・過冷却液体研究において中心的な役割を果たすと期待されている. 本講演では新しい動的 DFT の射影演算子理論からの導出を紹介する. また空間固定された粒子を含む Molecular dynamics について報告する.

1 密度汎関数理論 (DFT) – 動的DFTの新しい導出

1.1 射影演算子理論の復習

任意の力学変数を K 次元の縦ベクトル $\hat{\boldsymbol{A}} = (\hat{A}_1, \hat{A}_2, ..., \hat{A}_K)^T$ とすると $\hat{\boldsymbol{A}}$ は一般化ランジェバン方程式

$$d\hat{\boldsymbol{A}}(t)/dt = i\Omega \cdot \hat{\boldsymbol{A}}(t) - \int_0^t ds\Psi(t-s) \cdot \hat{\boldsymbol{A}}(s) + \hat{\boldsymbol{R}}(t) \tag{1}$$

を満足し, ダンダム力 $\hat{\boldsymbol{R}}(t)$ と記憶関数 $\Psi(t)$ については (1) 直交性 : $(\hat{\boldsymbol{R}}(t), \hat{\boldsymbol{A}}) = 0$ (2) 第2種の揺動散逸定理 : $\Psi(t) = (\hat{\boldsymbol{R}}(t), \hat{\boldsymbol{R}}) \cdot (\hat{\boldsymbol{A}}, \hat{\boldsymbol{A}})^{-1}$ を満たす.

もし $\hat{\boldsymbol{A}}$ が slow veriable のとき, その巾もやはり slow variable と考えられ, 非線形なランジェバン方程式を考えることが必要になる. (mode-coupling)

$$\hat{g}_a = \delta(\hat{\boldsymbol{A}} - \boldsymbol{a}) = \Pi_{i=1}^K \delta(\hat{A}_i - a_i) \tag{2}$$

$$d\hat{g}_a(t)/dt = i\int d\boldsymbol{a}'\Omega[\boldsymbol{a}, \boldsymbol{a}'] \cdot \hat{g}_{a'}(t) + \int_0^t \int d\boldsymbol{a}'\Psi[\boldsymbol{a}, \boldsymbol{a}', t-s] \cdot \hat{g}_{a'}(s) + R_a(t) \tag{3}$$

(1) K 次元空間での和, 例えば $\sum_{k=1}^{k=K}$ は $\Pi_{k=1}^K \int da'_k$ となる.

$$g(\boldsymbol{a}, t) = \int d\Gamma \hat{g}(\boldsymbol{a}) P(\Gamma, t) \tag{4}$$

(2) $g[\boldsymbol{a}, t]$ に対するランダム力のない式 (3) をフォッカープランク方程式と呼ぶ.

(3) マルコフ近似: $\Psi(\boldsymbol{a}, \boldsymbol{a}', t) \simeq \Psi(\boldsymbol{a}, \boldsymbol{a}', 0)\tau\delta(t)$

*〒 606-8501 京都市左京区吉田本町
†E-mail: munakata@amp.i.kyoto-u.ac.jp
‡E-mail: kin@amp.i.kyoto-u.ac.jp

1.2 density fluctuations と self-motion

密度場 $\hat{n}(\boldsymbol{r})$ とその分布関数 $\hat{g}[n]$ を考える.

$$\hat{n}(\boldsymbol{r}) = \sum_{i=1}^{N} \delta(\boldsymbol{r}_i - \boldsymbol{r}), \quad \hat{g}[n] = \Pi_\alpha \delta(\hat{n}(\boldsymbol{r}_\alpha) - n(\boldsymbol{r}_\alpha)) \tag{5}$$

ここに $\boldsymbol{r}_\alpha$ は空間の固定された点を表し, α を変化させると全空間を覆うと考える.

$$g_{eq}[n] \equiv \int d\Gamma \hat{g}[n] P_{eq}(\Gamma) \equiv \langle \hat{g}[n] \rangle = \exp(\beta F_N - \beta F[n]) \tag{6}$$

$$\partial g[n,t]/\partial t = -\int d\boldsymbol{r}_\alpha \delta/\delta n(\boldsymbol{r}_\alpha) J[n] \tag{7}$$

$$J = D\nabla_\alpha n(\boldsymbol{r}_\alpha)[\nabla_\alpha \delta g[n]/\delta n(\boldsymbol{r}_\alpha) + g[n]\beta\nabla_\alpha \delta F[n]/\delta n(\boldsymbol{r}_\alpha)] \tag{8}$$

高密度液体においては密度場のみがゆっくりと時間変化すると考えられ, これへの射影を全て引き去ったことから記憶関数は短い時間 τ で decay すると考えており, この意味で D を裸の拡散係数と呼ぶことができる. これはこれまで多くの人に提案されている動的DFTと一致する [1].

N-粒子系に 1 つの blue particle を加え $(N+1)$ 粒子系を考えると, blue particle の密度場の分布関数の時間発展は以下のようになる.

$$\hat{g}_0[n_0] = \Pi_\alpha \delta(\hat{n}_0(\boldsymbol{r}_\alpha) - n_0(\boldsymbol{r}_\alpha)). \tag{9}$$

$$\partial g_0[n_0,t]/\partial t = -\int d\boldsymbol{r}_\alpha \delta/\delta n_0(\boldsymbol{r}_\alpha) J_0[n] \tag{10}$$

$$J_0 = D\nabla_\alpha n_0(\boldsymbol{r}_\alpha)[\nabla_\alpha \delta g_0[n_0]/\delta n_0(\boldsymbol{r}_\alpha) + g_0[n]\beta\nabla_\alpha \delta F_0[n]/\delta n_0(\boldsymbol{r}_\alpha)] \tag{11}$$

$$g_{eq}[n_0] \equiv \langle \hat{g}_0[n_0] \rangle = \exp(\beta F_0 - \beta F_0[n_0]) \tag{12}$$

同様に N-粒子運動については以下のように与えられる.

$$\hat{g}[n,n_0] = \Pi_\alpha \delta(\hat{n}(\boldsymbol{r}_\alpha) - n(\boldsymbol{r}_\alpha))\delta(\hat{n}_0(\boldsymbol{r}_\alpha) - n_0(\boldsymbol{r}_\alpha)) \tag{13}$$

$$\partial g[n,n_0,t]/\partial t = -\int d\boldsymbol{r}_\alpha \{\delta/\delta n(\boldsymbol{r}_\alpha) J[n,n_0] + \delta/\delta n_0(\boldsymbol{r}_\alpha) J_0[n_0,n]\} \tag{14}$$

$$J[n,n_0] = D\nabla_\alpha n(\boldsymbol{r}_\alpha)[\nabla_\alpha \delta g[n,n_0]/\delta n(\boldsymbol{r}_\alpha) + g[n,n_0]\beta\nabla_\alpha \delta F_{N+1}[n,n_0]/\delta n(\boldsymbol{r}_\alpha)] \tag{15}$$

$$J_0[n_0,n] = D\nabla_\alpha n_0(\boldsymbol{r}_\alpha)[\nabla_\alpha \delta g[n,n_0]/\delta n_0(\boldsymbol{r}_\alpha) + g[n,n_0]\beta\nabla_\alpha \delta F_{N+1}[n,n_0]/\delta n_0(\boldsymbol{r}_\alpha)] \tag{16}$$

1.3 まとめ

一般に動的な DFT と呼ばれる構造を DFT 以外の枠組から導いた. これは thermal activation を含む記述になっておりガラスへの応用を視野に入れている. 自由エネルギーについては従来の DFT のものを近似として利用することも考えているが, 他にも可能性があることを指摘しておく.

2 Molecular dynamics – 拘束系の MD

これまで数多くのシミュレーションによってガラス・過冷却液体の性質について調べられている. その一方で実験においては薄膜や多孔質媒体に閉じ込めるなど拘束されたガラス実験がなされ, バルクとは異なる性質について明らかにされつつある [2]. このように様々な条件で拘束された状況下の性質を調べることでガラス特性の理解を深めることは興味深い方法である. そこで拘束系のシミュレーションの一例として, 過冷却液体に空間固定された粒子が含まれる場合どのように体系の性質が変化するかを調べ, 固定粒子とガラス化過程の関係を明らかにする.

2.1 シミュレーションと結果

過冷却液体のモデルとしてよく取り上げられる 2 成分 (成分 : A, B) ソフトコア粒子混合物を用いた [3]. 粒子数 $N = 1000$, 全数密度 $\rho = 0.8$ を一定として, 液体から過冷却液体まで様々な温度 ($0.306 \leq T \leq 0.772$) の状態を用意する. 各状態においてシミュレーションのある時点で体系を構成する粒子の w_d% ($w_d \leq 5$) をランダムに空間固定し, その後の静的および動的性質を調べた. 静的性質を見るために 成分 A に関する動径分布関数 $g_{AA}(r)$

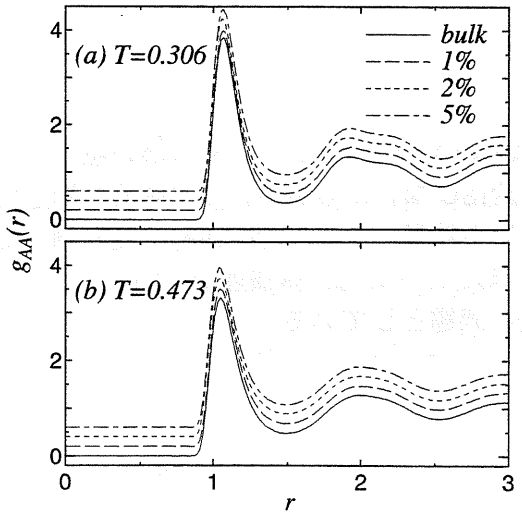

Fig. 1: $T = 0.306$(a), 0.473(b) における動径分布関数 $g_{AA}(r)$.

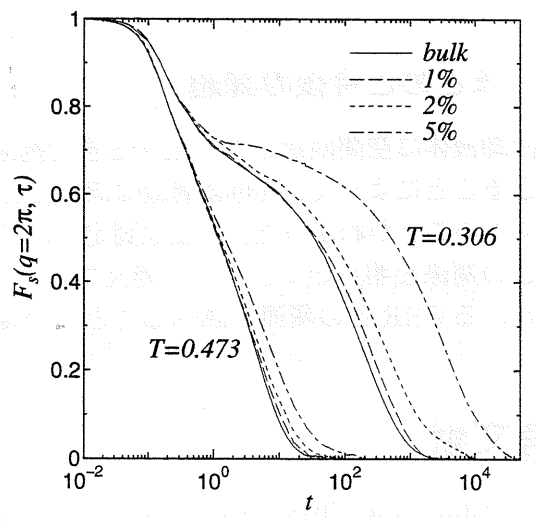

Fig. 2: 成分 A に関する中間散乱関数 $F_s(q = 2\pi, t)$.

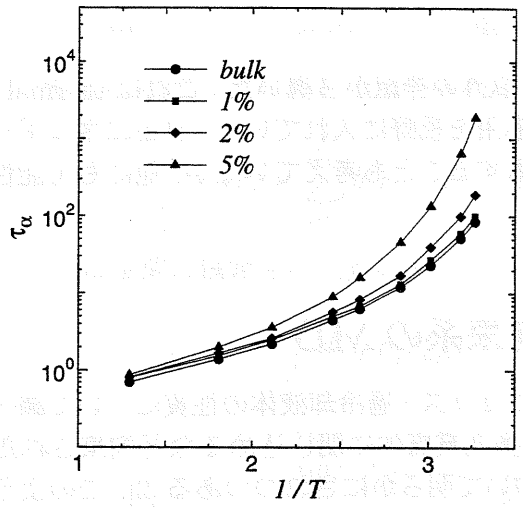

Fig. 3: 緩和時間 τ_α の温度依存性.

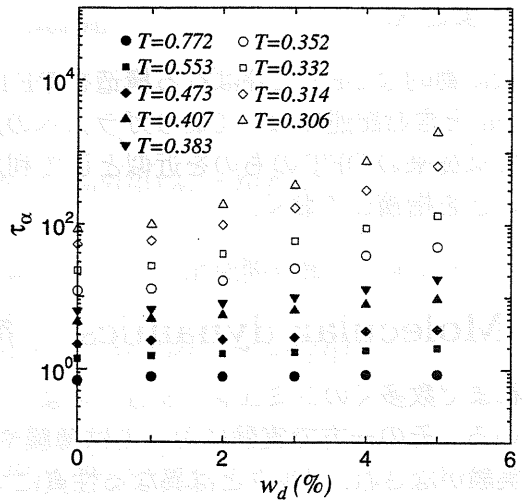

Fig. 4: 緩和時間 τ_α の固定粒子数依存性.

を各温度で求めた. Fig.1 に $T = 0.306$(a) と $T = 0.473$(b) の結果が示されているが, 固定されている粒子数に依らずバルクのものとほとんど変化がないことがわかった. またこのことを液体から過冷却液体まであらゆる温度で確認している. さらに動的性質を調べるために各温度で成分 A に関する中間散乱関数のセルフ部分 $F_s(q = 2\pi, t)$ の時間発展を求め, $T = 0.306$, 0.473 の結果を Fig.2 に示した. 液体状態から過冷却状態になるにつれ固定された粒子を含む体系の構造緩和が遅くなる様子を見ることができる. 緩和時間を $F_s(q = 2\pi, t = \tau_\alpha) = e^{-1}$ なる τ_α で定義し, その温度依存性を見たものが Fig.3 である. また緩和時間の固定粒子数による変化を見るために Fig.4 には各温度における τ_α を w_d の関数としてプロットした. これらからバルクのものに比べより多くの固定粒子を含む体系が, 特に過冷却状態で緩和時間が遅くなることがわかる.

2.2 まとめと今後の課題

過冷却液体に空間固定された粒子を含む拘束系の MD を行った. いくつかの粒子が空間固定さることによって, 静的な構造はほとんど変化しないにもかかわらず体系の構造緩和が遅くなることがわかった. 今後は固定されている粒子のまわりでの運動特性を調べ緩和過程との関係を明らかにしたいと考えている. またさらに自由体積理論, Adam–Gibbs 理論における CRR との関連を調べることも今後の課題としている.

参考文献

[1] T. Munakata, Phys. Rev. E **50**, 2347 (1994).

[2] *Proceedings of International Workshop on Dynamics in Confinement*, J. Phys. IV, **10**, Proceedings Pr7 (2000).

[3] R. Yamamoto and A. Onuki, Phys. Rev. E **58**, 3515 (1998).

Statistical mechanics of two hard disks in a rectangular box

Toyonori Munakata,
Department of Applied Mathematics and Physics,
Kyoto University, Kyoto 606, Japan
Gang Hu,
Department of Physics, Beijing Normal University,
the People's Republic of China

Abstract

A system of two hard disks in a rectangular box is studied based on the exact partition function and equilibrium distribution functions of particles. Box-size dependence of some quantities of interest, such as pressure and the particle distribution functions, is investigated and in particular the negative compressibility of the van der Waals type and the corresponding phase transition are analysed in detail. This system turns out to have rich structures which are related to the ergode-nonergode transitions in this system.

As is well known, chaos and ergodicity[1,2] serve as a bridge linking mechanics and statistics. This bridge is not limited to many-body systems, a main field for application of statistical mechanics. Currently some few-body systems gather considerable attention in this regard and for few-body hard

core(or disk) systems, entropy[3], the thermodynamic second law[4], and a phase transition[5] are discussed to mention a few.

We consider a system composed of two identical hard disks put in a rectangular box, which was studied by Awazu[5] with a molecular dynamics(MD) method and a liquid-solid like transition[6] with negative compressibility was observed to exist. It is noted however that without explicit analysis the understanding of the mechanism underlying the interesting behavior is not complete and the purpose of this paper is to study the system by entirely analytical computation and understand the van der Waals features in the large density case statistical mechanically.

We denote the diameter of a hard disk by d and a horizontal(vertical) length of the rectangular box by $l_x + d(l_y + d)$. It is remarked that as l_x is decreased from above d to below d, the system naturally shows an ergode-nonergode transion, in which a particle occupying the upper part of the box is kept from going into the lower part when l_x becomes smaller than d. In order to take into account the particle-wall interaction, we introduce the coordinate system (x, y), in which x and y can take values in the range $0 \leq x \leq l_x$ and $0 \leq y \leq l_y$, respectively. With use of (x, y), the distribution function of the position coordinates $\{x_i, y_i (i = 1, 2)\}$ is simply given by $p(x_1, y_1; x_2, y_2) = 1/Z_c$ for $R \equiv [(x_1 - x_2)^2 + (y_1 - y_2)^2]^{1/2} \geq d$ and $p(x_1, y_1; x_2, y_2) = 0$ for $R < d$. Here the configurational partition function $Z_c(l_x, l_y)$ normalizes the probability distribution function by $\int dx_1 dx_2 dy_1 dy_2$ $p(x_1, y_1; x_2, y_2) = 1$.

Let us consider the probability distribution functions $f(x)$ and $g(y)$ for

the relative coordinates $x = x_2 - x_1$ and $y = y_2 - y_1$, which were numerically obtained before.[5] For example $f(x)$ is defined by $f(x) \equiv \int dx_1 dx_2 dy_1 dy_2$ $p(x_1, y_1; x_2, y_2)\delta(x - [x_2 - x_1])$. It is convenient to divide the space (l_x, l_y) into four regions, $l_x \geq d, l_y \geq d$(region I), $l_x \geq d, l_y < d$(region II), $l_x < d, l_y \geq d$(region III), and $l_x < d, l_y < d$(region IV). Simple symmetry consideration reveals that in the region I and IV, $f(x)$ and $g(y)$ are even and we have

$$f_I(x|l_x, l_y) = g_I(x|l_y, l_x), \qquad f_{IV}(x|l_x, l_y) = g_{IV}(x|l_y, l_x), \tag{1}$$

where size-dependence of the functions f and g is shown explicitly. In the regions II, $g(y)$ is even and $f(x)$ is to be treated only for e.g. $l_x \geq x \geq 0$ since two particles can not change their left-right relationship in the course of time. Symmetry consideration tells us that

$$g_{III}(y|l_x, l_y) = f_{II}(y|l_y, l_x), \qquad g_{II}(y|l_x, l_y) = f_{III}(y|l_y, l_x). \tag{2}$$

We start from the region I. When $l_x \geq x \geq d$, the contribution to $f(x)$ from $\int dy_1$ and $\int dy_2$ is l_y^2 and from the relation $0 \leq x_1 \leq l_x - x$, the contribution from x_1 integration is $(l_x - x)$. Thus we have

$$f(x) = l_y^2(l_x - x)/Z_c. \qquad (d \leq x \leq l_x) \tag{3}$$

When $0 \leq x \leq d$ and if we confine the contribution to $f(x)$ from the region $y_1 \leq y_2$, we have the factor $l_y - [y_1 + (d^2 - x^2)^{1/2}]$ from y_2 integration and this is first integrated from 0 to $l_y - (d^2 - x^2)^{1/2}$ over y_1 and then multiplied by $l_x - x$ as the contribution from x_1 integration. Finally this is to be multiplied

by 2 since the region $y_1 \geq y_2$ gives precisely the same contribution as above to $f(x)$. Thus immediately we have

$$f(x) = (l_x - x)(l_y - (d^2 - x^2)^{1/2})^2/Z_c. \quad (0 \leq x \leq d) \tag{4}$$

Noting that $f(x)$ is even in x, we obtain Z_c from the condition $\int_{-l_x}^{l_x} f(x) = 1$ to be

$$\begin{aligned} Z_c(l_x, l_y) &= l_y^2(l_x - d)^2 + 2\int_0^d (l_y - (d^2 - y^2)^{1/2})^2(l_x - y)dy \\ &= l_x^2 l_y^2 - \pi d^2 l_x l_y + (4/3)(l_x + l_y)d^3 - d^4/2. \end{aligned} \tag{5}$$

In the region II $f(x)$ is considered only in the region $0 \leq x \leq l_x$ as noted before. New aspect is that x can not be smaller than $x_{min} \equiv (d^2 - l_y^2)^{1/2}$. In the region $d \leq x \leq l_x$, $f(x)$ is given as before by Eq. (3). When $x_{min} \leq x \leq d$, $f(x)$ is given by Eq. (4), that is

$$f(x) = (l_x - x)(l_y - (d^2 - x^2)^{1/2})^2/Z_c. \quad (x_{min} \leq x \leq d) \tag{6}$$

$$f(x) = 0 \quad (0 \leq x \leq x_{min}) \tag{7}$$

From the normalization condition $\int_0^{l_x} f(x)dx = 1$, we have

$$\begin{aligned} Z_c(l_x, l_y) &= l_y^2(l_x - d)^2/2 + 2\int_{\sqrt{d^2 - l_y^2}}^d (l_y - (d^2 - y^2)^{1/2})^2(l_x - y)dy \\ &= l_x^2 l_y^2/2 - l_y^4/12 + 2l_x d^3/3 + l_y^2 d^2/2 - l_x l_y d^2\theta \\ &- l_x(l_y^2 + 2d^2)(d^2 - l_y^2)^{1/2}/3, \end{aligned} \tag{8}$$

where $\sin\theta = l_y/d$. As l_y approaches d from below d in Eq. (8) and from above d in Eq. (5), we notice that $Z_c(l_x, l_y \uparrow d) = Z_c(l_x, l_y \downarrow d)/2$, reflecting

the nonergode-ergode transition at $l_y = d$. As to the probability distribution function of $y \equiv y_2 - y_1$, it is easily obtained that

$$g(y) = (l_y - |y|)(l_x - (d^2 - y^2)^{1/2})^2/(2Z_c). \quad (0 \leq |y| \leq l_y) \tag{9}$$

The results for the region III is easily obtained from Eq. (2).

Finally let us consider the region IV. If $l_x^2 + l_y^2 \leq d^2$, the box can contain only one particle. For $l_x^2 + l_y^2 > d^2$, we have four ergodic components(if we regard two particles distinguishable), in each of which two particles are distributed along one of two diagonal lines of the box. The distribution function $f(x)$ of the relative coordinate $x_2 - x_1 (> 0)$ is given by

$$f(x) = (l_x - x)(l_y - (d^2 - x^2)^{1/2})^2/(2Z_c). \quad ((d^2 - l_y^2)^{1/2} \leq x \leq l_x). \tag{10}$$

$$f(x) = 0. \qquad (0 \leq x \leq (d^2 - l_y^2)^{1/2}). \tag{11}$$

Z_c is calculated from $\int_0^{l_x} f(x) = 1$ to have

$$\begin{aligned} Z_c(l_x, l_y) &= (1/2)\int_{\sqrt{d^2 - l_y^2}}^{l_x} (l_y - (d^2 - y^2)^{1/2})^2 (l_x - y)dy \\ &= l_x^2 l_y^2/4 - (l_x^4 + l_y^4)/24 + (l_x^2 + l_y^2)d^2/4 + l_x l_y d^2(\pi/2 - \theta_1 - \theta_2)/2 \\ &- (d^2 - l_y^2)^{1/2}[d^2 l_x/3 + l_x l_y^2/6] \\ &- (d^2 - l_x^2)^{1/2}[d^2 l_y/3 + l_y l_x^2/6] + d^4/8, \end{aligned} \tag{12}$$

where $\sin\theta_1 = l_x/d$ and $\sin\theta_2 = l_y/d$. It is easily confirmed that as l_x goes to d in Eq.(8), the Z_c is twice the Z_c obtained from Eq.(12) in the same limit. This is due to the ergode-nonergode transition additional to the one already mentioned just below Eq. (8). It is noted however that there is no discontinuity in pressure, defined below by Eq. (14), as readily seen from Z_c

expressed by integral forms in Eqs. (5), (8), and (12).

Now we turn to the equation of state of our system. The configurational part of the entropy S_c is given by

$$S_c(l_x, l_y) = k_B \ln Z_c(l_x, l_y), \tag{13}$$

where k_B denotes the Boltzmann constant. Pressure on the wall is expressed by

$$p_x(l_x, l_y) = T\partial S_c/\partial l_x, \qquad p_y(l_x, l_y) = T\partial S_c/\partial l_y, \tag{14}$$

with T temperature of the system. For hard-disk systems T determines only a time scale and hereafter we put $k_B = 1$, and $T = 1$ for simplicity. It is remarked that our system is thermodynamically characterized by (l_x, l_y) and from symmetry $p_x(l_x, l_y) = p_y(l_y, l_x)$.

The unisotropic pressure obtained by MD experiments[5] in some part of (l_x, l_y) region($l_y > d$) was confirmed to be consistent with our analytic results Eq. (14). As examples, some p_x for $l_y > d$ are shown in Fig.1 as a function of l_x. We notice that the pressure p_x on the side(left or right) walls shows the van der Waals characteristics for $d < l_y < l_{y,c}$ where $l_{y,c}(= 2.106d)$ denotes the (upper) critical value of l_y to be discussed later. In contrast, p_y only monotonously decreases with l_x for $l_y > d$.

Usually the van der Waals behavior is ascribed to an interplay between the short-range repulsion and the long-range attraction in the interatomic potential.[7] The long-range attraction tends to reduce the pressure on the wall by means of a slight density increase inside the container of the gas. The hard-disk system shown in Fig.1 is highly compressed and inhomogeneous.

In Fig.2 we plot, for $l_y/d = 1.2$, the probability distribution function of x coordinate of a particle $n_x(x)$, defined by $n_x(x) \equiv \int dx_1 dy_1 dy_2 p(x_1, y_1; x, y_2)$. In this compact packing generally, particles are located near the wall and the central part of the box is less populated. As l_x/d decreases from 1.2 to 1.0, the $n_x(x = l_x)$, that is, the density at the side wall, first increases and then decreases, showing a (local) maximum around $l_x/d \simeq 1.1$. This property of local density variation is in accord with the variation of pressure p_x shown in Fig.1($l_y/d = 1.2$). Thus we consider that the density at a wall, which is determined through complicated packing of hard disks in a small rectangular box, is the main factor for the van der Waals behavior of p_x in Fig.1. In contrast to $n_x(x = l_x)$, $n_y(y = l_y)$ turned out to increase monotonously as l_x/d is decreased from 1.2 to 1 for $l_y/d = 1.2$. It is noted that whenever we observed the van der Waals behavior we simultaneously observed the similar nonmonotonous behavior of particle density at the wall.

Qualitatively we may understand this van der Waals behavior as follows: First let us express p_x as

$$p_x = (1 - W)p_{n-con} + W p_{con}, \tag{15}$$

where W denotes the probability of two particles being contact each other along the x axis, i.e., $|x_2 - x_1|$ is around d, and p_{con} the pressure in this situation which is larger than p_{n-con} for the noncontact case. As l_x becomes small from $l_x >> d$, p_x increases due to the increase of both p_{n-con} and p_{con}. Under further compression, p_x decreases first due to drastic decrease of W and $W p_{con}$ and then increases due to increase of $p_{n-con}(W \simeq 0)$, resulting in the van der Waals behavior. Similar argument, if applied to the l_x depen-

dence of p_y, can explain the monotonous behavior mentioned above.

We now proceed to the region $l_y < d$, which was not investigated before. Just as for the case $l_y > d$, we observed the van der Waals behavior for $p_x(l_x, l_y)$ as shown in Fig. 3. This is also qualitatively explained based on Eq. (15). That is, under a closely packed situation, the van der Waals behabior may result from the change in packing mechanism, which accompanies the ergode-nonergode transition. This is in sharp contrast with the many-body hard-core system for which there is no distinction between a gas and a liquid. In the region $l_y < d$, there is an unstable region, in which the compressibility from p_x becomes negative.(see Fig.3) As for p_y we only observed an monotonous gas-like behavior for variation in l_x.

Collecting the results presented above for $p_x(l_x, l_y)$, we show in Fig. 4 the phase diagram in the (l_x, l_y) plane. The two curves $C1, C2$ from $(d, l_{y,c})$ to $(d, 0)$ determine the unstable region, in which the compressibility becomes negative. One may call the region A, which is either to the right of $C1$ or above the line $l_y = l_{y,c}$, a gas phase and the region B, which is left to $C2$, below the line $l_y = l_{y,c}$ and above S, a liquid phase. Inside the curve $S = (l_x, l_y) : l_x^2 + l_y^2 = d^2$, the system can contain only one particle. However in the region B, if we distinguish a fully constrained region $B' : l_x < d, l_y < d$ from the remaining half-constrained region $l_y > d$ in B, one may call the system in B' a solid phase and the transition below the line $l_y < d$ becomes the gas-solid one. We note that this phase diagram comes from the system response, more explicitly, the response of p_x to l_x variation. p_y does not show any instability. If we study the response to l_y variation, then p_y shows

instability and we only need to change the coordinates from the symmetry mentioned just below Eq. (14).

Finally we comment on the probability distribution functions $f(x)$ and $g(y)$ for the relative positions. As a situation interesting from the viewpoint of application of the analytic expression for these functions, we consider l_y/d is larger than 1 and l_x/d becomes gradually small and approaches 1. In order for the particle located in the upper part to exchange position with the one in the lower part, the transition state, $y \equiv y_2 - y_1 = 0$ must be crossed. If we put $l_x/d = 1 + \epsilon$ with $0 < \epsilon << 1$, it is readily obtained from Eqs.(1) and (4) that $g(y = 0)$ approaches ϵ^2, showing that it takes a long time of the order ϵ^{-2} for two particles to exchange their relative(upper-lower) position and this results in the slow relaxation observed in Ref. [5].

In this paper we considered a system composed of two hard disks based on analytic expressions for the partition function and some probability distribution functions. A system of two particles, which shows ideal or low-density gas properties if put in a box with large volume or under the periodic boundary condition, bahaves quite differently in a compressed situation and shows a gas-liquid or a liquid-solid like transition. Packing is one of the most important factors controlling properties of dense liquids[8] and amorphous substances(glass).[9,10] Thus we believe that investigation of properties of a few-body system packed in a small box might give important insights on condensed matter physics. Along this line some properties of a three-disk system and a thin two dimensional N-particle system will be dicussed in near future.

References

[1] E. Ott, *Chaos in Dynamical Systems*(Cambridge University Press, Cambridge, 1993).

[2] L. E. Reichl, *The Transition to Chaos*(Springer-Verlag, Berlin, 1992).

[3] Z. Zheng, G. Hu, and J. Zhang, Phys. Rev. E **53** 3246 (1996).

[4] Gang Hu, Zhigang Zheng, Li Yang, and Wei Kang, Phys. Rev. E. **64** 045102(R) (2001).

[5] A. Awazu, Phys. Rev. E **63**, 032102 (2001).

[6] This had better be called a gas-liquid transition for reasons to be clarified later.

[7] L. E. Reichl, *A Modern Course in Statistical Physics*, (University of Texas Press, Austin, 1980).

[8] J. P. Hansen and I. R. MacDonald, *Theory of Simple Liquids*, (Academic Press, New York, 1986).

[9] *Liquids, Freezing and the Glass Transition*, ed. by J. P. Hansen, D. Levesque, and J. Zinn-Justin. (North-Holland, Amsterdam, 1989)

[10] E. Donth, *The Glass Transition*,(Springer Verlag, Berlin, 2001).

Figure Captions

Fig.1 Pressure on the vertical wall $p_x(l_x, l_y)$ for various l_y values as functions of l_x. From the upper curve, l_y/d =1.2, 1.4, 1.6, 1.8, 2.0 and 2.2. Temperature T and the Boltzmann constant are both set equal to one and the pressure is non-dimensional.

Fig.2 Density profile $n_x(x)$ for $l_y/d = 1.2$ and l_x in the range between 1.0 and 1.2 with the increment $\Delta l_x = 0.02$. It is noted that x is in the range $0 < x < l_x$.

Fig.3 l_x dependence of p_x for $l_y/d = 0.75$(full curve) and $l_y/d = 0.85$ (dashed curve).

Fig.4 Phase diagram in the (l_x, l_y) space.

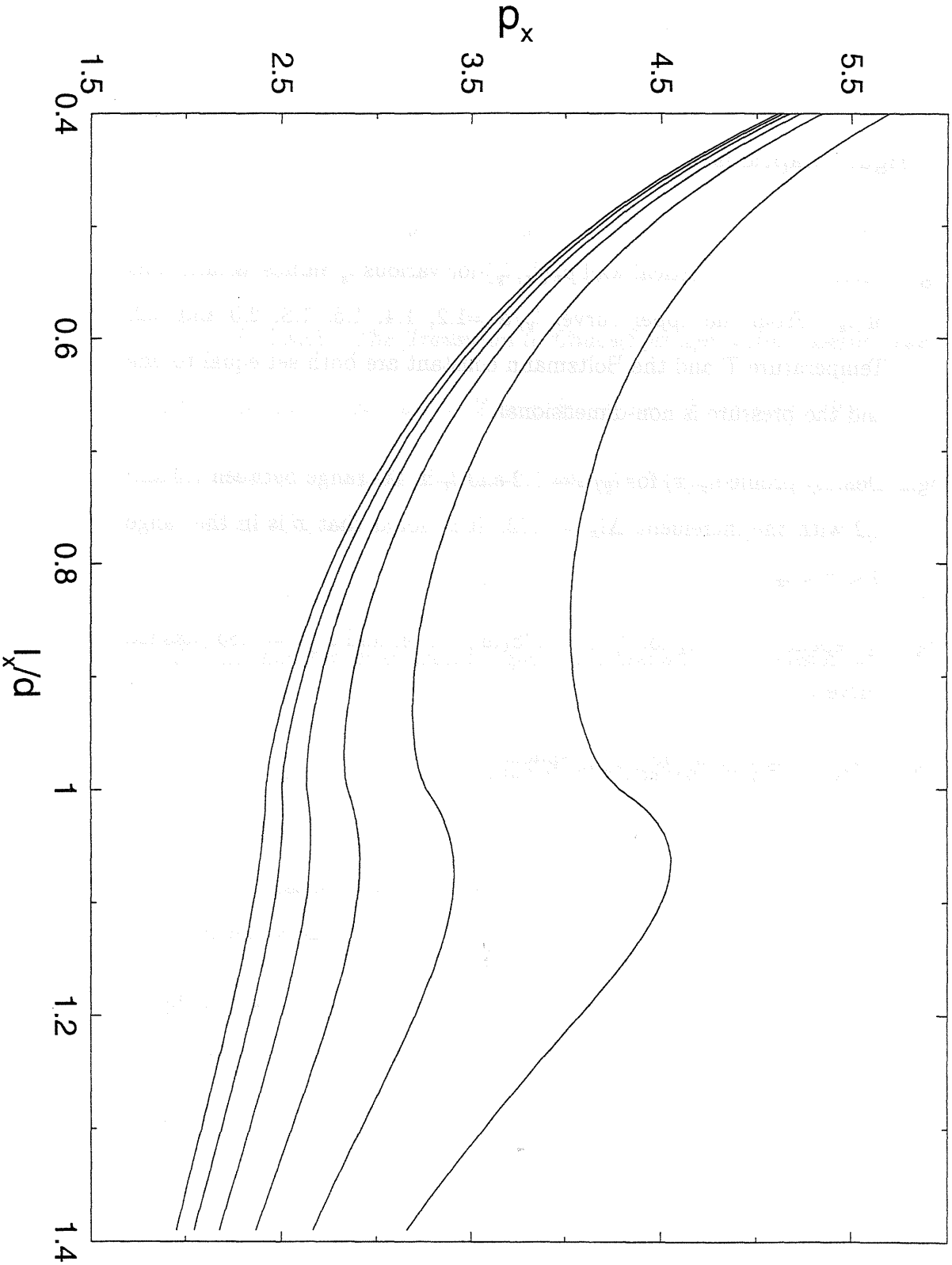
ρ_x
1.5
2.5
3.5
4.5
5.5
0.4
0.6
0.8
1
1.2
1.4
l_χ/d

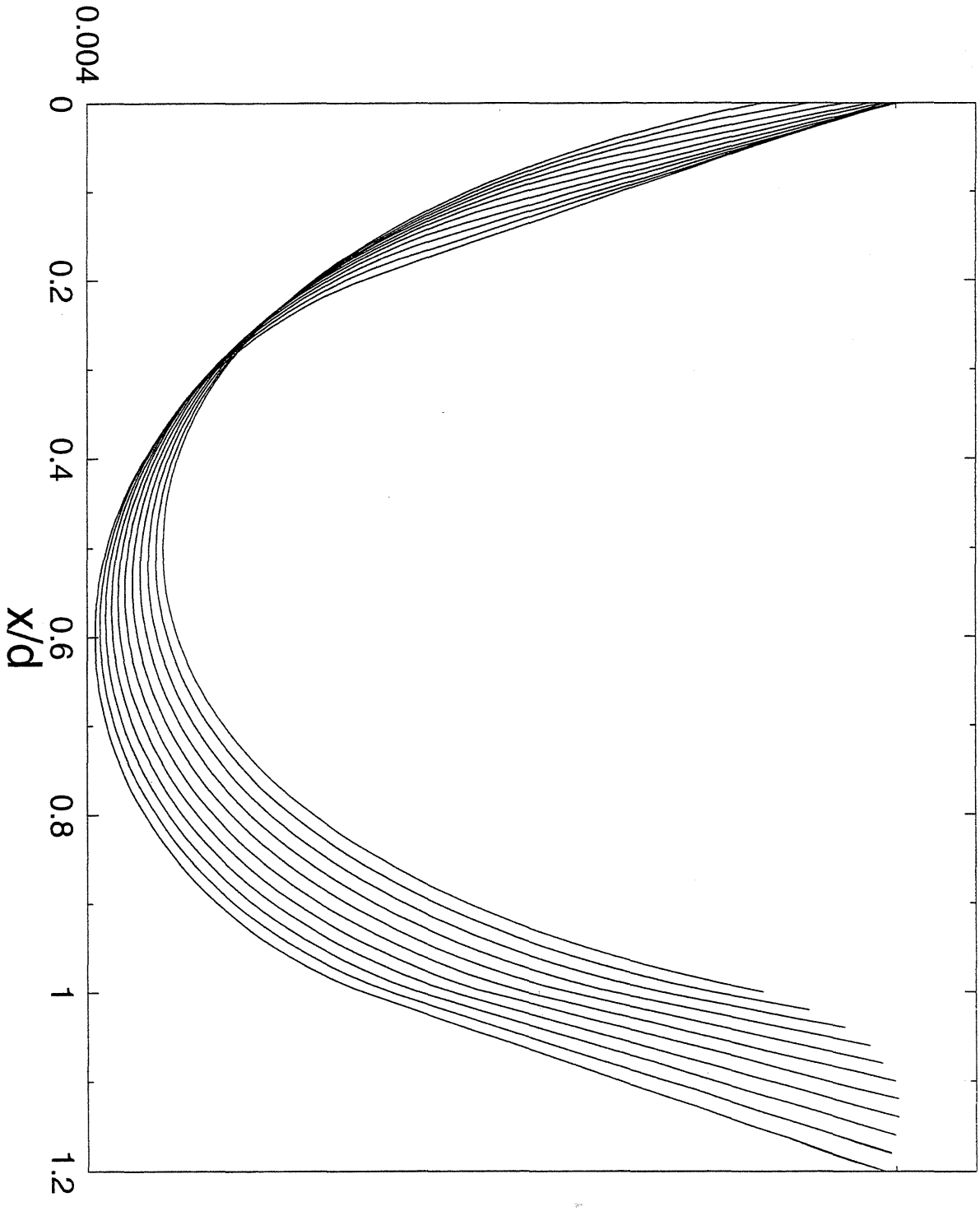
$n_x(x)$
0.004
0
0.2
0.4
0.6
0.8
1
1.2
x/d

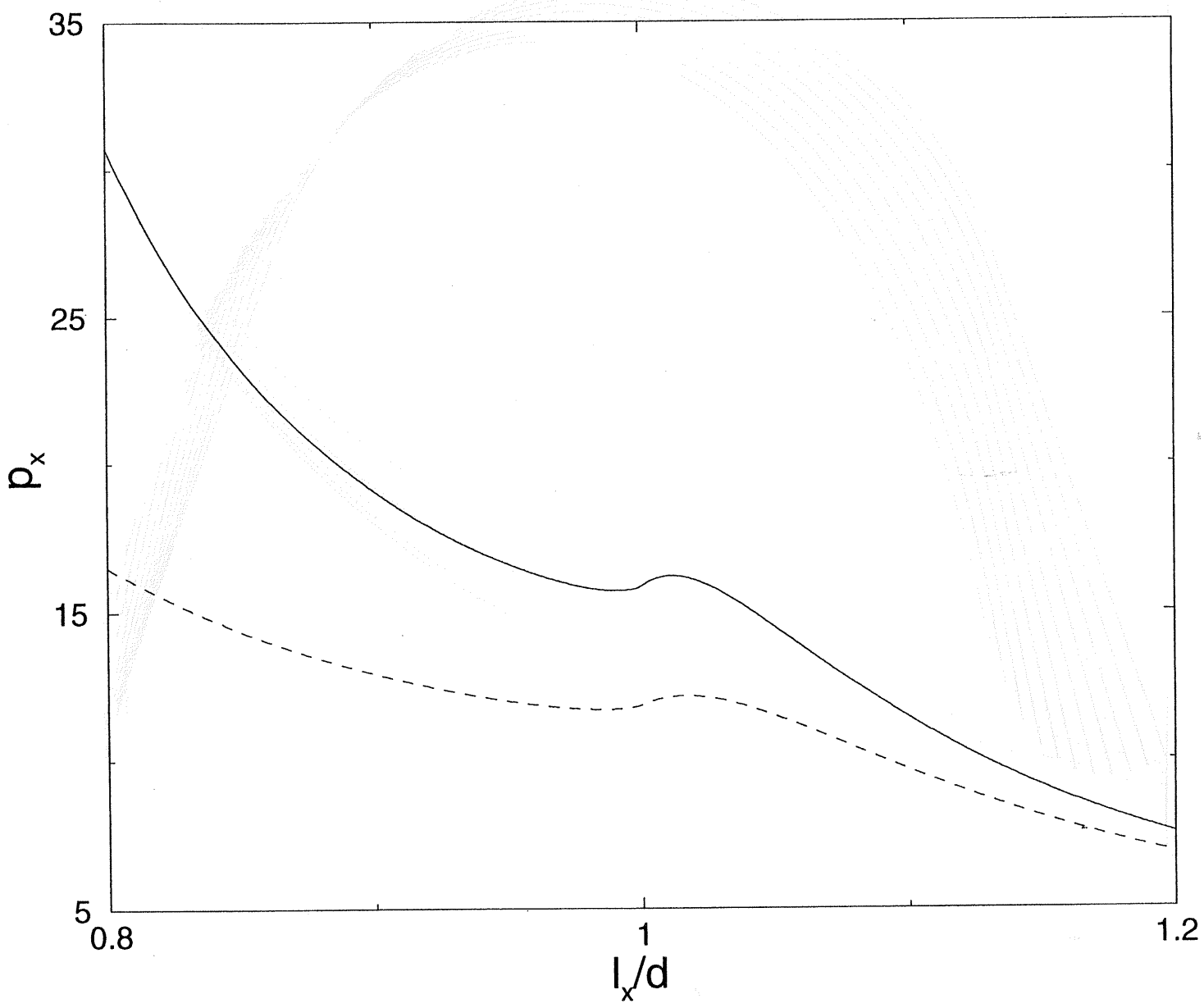
35
25
15
5
p_x
0.8
1
1.2
l_x/d

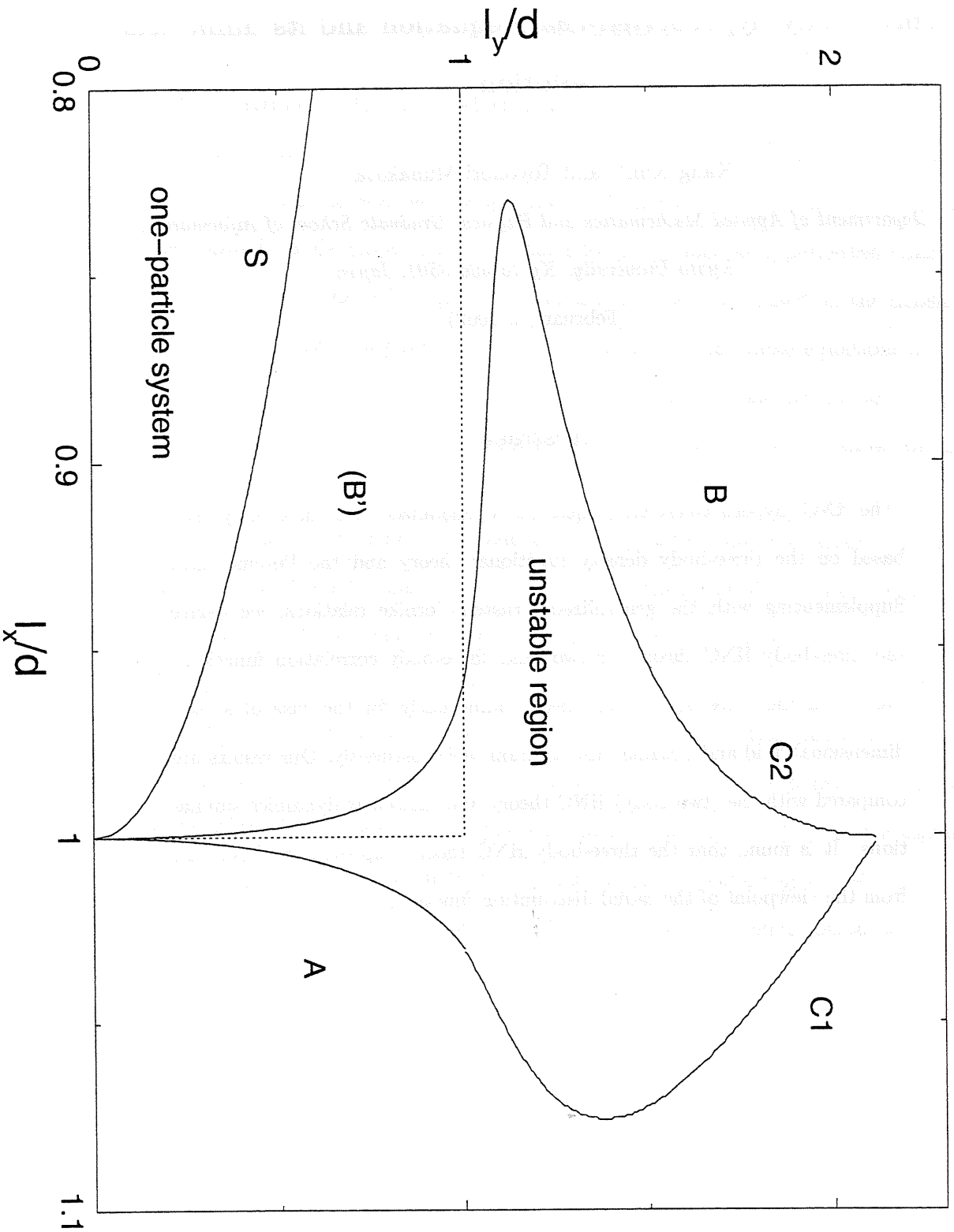
l_y/d
0
1
2
l_x/d
0.8
0.9
1
1.1
one–particle system
S
(B')
B
unstable region
C2
A
C1

Three-body hypernetted-chain equation and its numerical solution

Kang Kim* and Toyonori Munakata†

Department of Applied Mathematics and Physics, Graduate School of Informatics, Kyoto University, Kyoto 606-8501, Japan

(February 4, 2002)

Abstract

The HNC (hypernetted-chain) equation is generalized at a three-body level based on the three-body density functional theory and the Percus' idea. Supplementing with the generalized Ornstein-Zernike relations, we derive the three-body HNC theory for two- and three-body correlation functions. We solved the three-body HNC theory numerically for the case of a one-dimensional fluid and obtained the solution self-consistently. Our results are compared with the (two-body) HNC theory and molecular dynamics simulations. It is found that the three-body HNC theory improves the HNC one from the viewpoint of the radial distribution function.

*E-mail:kin@amp.i.kyoto-u.ac.jp

†E-mail:munakata@amp.i.kyoto-u.ac.jp

I. INTRODUCTION

The pair distribution function, which is usually called the radial distribution function $g_2(r)$, plays a central role in characterizing structures of simple liquids [1]. The $g_2(r)$ has been obtained by neutron scattering experiments [1] or computer simulations [2]. Theoretically, there have been developed some equations for $g_2(r)$, such as hypernetted-chain (HNC) equation or Percus-Yevick (PY) equation to mention a few [1,3], based on the density functional theory (DFT) and diagram methods [1]. It is noted that these equations are usually of the form of integral equations and rather heavy numerical calculations are required to solve them, except for the PY equation for a hard-core system [1] which allows an analytic solution.

As an exact theoretical framework and also as a practical and convenient tool to study structure of liquids, the DFT has been playing an important role [4] in studies of the freezing [5], glass transition [6], molecular liquids [7], and so on. It is worth mentioning that the HNC equation for $g_2(r)$ can be derived from the DFT.

Let us consider a d-dimensional fluid system with an interaction potential $\phi(r)$. If one particle is located at the origin $\boldsymbol{r} = 0$ of the system, the one-particle density can be related, with the aid of the Percus' idea, to the pair-correlation function [8]. That is, the equilibrium density $n(\boldsymbol{r})$ represents $n_0 g_2(r)$ with the normalization condition $g_2(r) \to 1$ as $r \to \infty$. According to the variational principle of the DFT, we obtain an equation to determine the equilibrium density $n(\boldsymbol{r})$,

$$\frac{\delta F[n]}{\delta n(\boldsymbol{r})} + \phi(r) = \mu, \tag{1}$$

where $F[n]$ is the free energy functional of a fluid and μ represents a chemical potential.

The free energy functional $F[n]$ is divided into the ideal gas part F_{id} and the interaction part F_{ex}. F_{id} is given exactly as the first term on the right hand side of Eq. (2), and F_{ex} is expressed as an expansion around the uniform liquid state $n(\boldsymbol{r}) = n_0$. Then $F[n]$ is given by,

$$F[n] \equiv F_{id} + F_{ex}$$
$$= k_B T \int d\boldsymbol{r} n(\boldsymbol{r}) \{\ln[n(\boldsymbol{r})\Lambda^d] - 1\} - k_B T \sum \frac{1}{M!} \int d\boldsymbol{r}_1 \cdots \int d\boldsymbol{r}_M$$
$$\times \{C_M(\boldsymbol{r}_1, \cdots, \boldsymbol{r}_M)\}\{n(\boldsymbol{r}_1) - n_0\} \cdots \{n(\boldsymbol{r}_M) - n_0\}, \tag{2}$$

where Λ and C_M denote the thermal wavelength and the M-th order direct correlation function, respectively.

If F_{ex} is truncated after $M = 2$ as is usually done, we have the free energy functional

$$F[n] \simeq k_B T \int d\boldsymbol{r} n(\boldsymbol{r}) \{\ln[n(\boldsymbol{r})\Lambda^3] - 1\}$$
$$- \frac{k_B T}{2} \int d\boldsymbol{r} \int d\boldsymbol{r}' [n(\boldsymbol{r}) - n_0] C_2(|\boldsymbol{r} - \boldsymbol{r}'|)[n(\boldsymbol{r}') - n_0], \tag{3}$$

which was employed by Ramakrishnan and Yussouff to investigate a liquid-crystal transition [5]. The $C_2(r)$ is related to the two-body total correlation function $h_2(r) \equiv g_2(r) - 1$ by the Ornstein-Zernike (OZ) relation [1],

$$h_2(r) = C_2(r) + n_0 \int d\boldsymbol{r}' C_2(|\boldsymbol{r} - \boldsymbol{r}'|) h_2(r'). \tag{4}$$

We note that the second-order direct correlation function $C_2(r)$ multiplied by $-k_B T$ can be interpreted as the two-body effective interaction.

Inserting the free energy functional form (3) into the variational equation (1), we immediately obtain from $n(\boldsymbol{r}) = n_0 g_2(r)$

$$\ln g_2(r) = -\phi(r)/(k_B T) + n_0 \int d\boldsymbol{r}' C_2(|\boldsymbol{r} - \boldsymbol{r}'|) h_2(r'), \tag{5}$$

which is equivalent to the HNC equation [1]. The equation set (4) and (5) can be solved numerically to yield the theoretical expression for $g_2(r)$.

In our previous paper we approximated F_{ex} by including up to the M-th order terms in Eq. (2) ($M(> 2)$-body DFT) and derived the generalized HNC equation, which was to be supplemented with the up to M-th order Ornstein-Zernike relations to obtain a closed set of integral equations [10]. For the case of $M = 3$, we tried to solve the HNC theory and could present rather imperfect numerical results because of various difficulties in our numerical

calculations [10]. In similar efforts to understand and to take into account effects of higher order correlations in liquids, Verlet introduced the PY2 or HNC2 equation by extending the systematic functional expansion method due to Percus [9]. Similarly there have been several attempts to understand the three-body correlation in a fluid [11–13].

As is anticipated, it is a demanding task to obtain numerical solutions of integral equations including the three-body correlation function. The purpose of this paper is to try again numerical solutions of the three-body HNC theory and present more reliable numerical solution to enable evaluation of our three-body HNC theory. The organization of this paper is as follows. In Sec. II, we summarize the three-body HNC theory and in Sec. III, after explaining our method of numerical solutions, we present numerical results of two- and three-body correlation functions. Finally in Sec. IV we conclude this paper.

II. FORMALISM OF THREE-BODY HNC THEORY

In order to make this paper self-contained, here we briefly summarize $M = 3$ HNC (HNC3) theory and write down equations necessary for explanation of our numerical algorithm. For the case of $M = 3$, we have a set of equations to determine the two- and three-body correlation functions $g_2(1,2)$ and $g_3(1,2,3)$ with 1 denoting the position vector $\boldsymbol{r}_1$. As to $g_3(1,2,3)$, we can express it as $g_3(1,2,3) = g_1(2|1)g_1(3|1,2)$, where $g_1(3|1,2)$ represents the one-body distribution function at 3 when two particles are located at 1 and 2, and $g_1(2|1)$ is identical with the radial distribution function $g_2(1,2)$. According to our previous paper, the HNC3 theory consists of the following equations:

$$\begin{aligned}\ln g_1(2|1) &= -\phi(1,2)/(k_BT) + n_0 \int d1' C_2(1',2) h_1(1'|1) \\ &\quad + (n_0^2/2) \int d1' \int d2' C_3(1',2',2) h_1(1'|1) h_1(2'|1) \\ &\equiv -\phi(1,2)/(k_BT) + C^{(2)}(2|1) + B^{(2)}(2|1), \end{aligned} \tag{6}$$

$$\ln g_1(3|1,2) = -(\phi(1,3) + \phi(2,3))/(k_BT) + n_0 \int d1' C_2(1',3) h_1(1'|1,2)$$

$$+ (n_0^2/2) \int d1' \int d2' C_3(1',2',3) h_1(1'|1,2) h_1(2'|1,2)$$
$$\equiv -(\phi(1,3)+\phi(2,3))/(k_BT) + C^{(3)}(3|1,2) + B^{(3)}(3|1,2), \tag{7}$$

where $h_1(2|1) \equiv g_1(2|1) - 1$ and $h_1(3|1,2) \equiv g_1(3|1,2) - 1$. Here $C^{(m)}$ and $B^{(m)}$ $(m = 2, 3)$ are called a m-body convolution and bridge function, respectively [10]. Neglecting the $B^{(2)}$ in Eq. (6), we immediately obtain the usual (two-body) HNC equation (5). The $B^{(2)}$ represents the potential field at 2 produced by particles at $1'$ and $2'$ through the $C_3(1',2',2)$. Similarly to the C_2, the third-order direct correlation function C_3 multiplied $-k_BT$ can be regarded as the effective three-body interaction.

We next turn to the generalized OZ relations between the functions g_2, g_3 and C_2, C_3. It is useful to express the two- and three-body OZ relations in Fourier space because of their convolution structures:

$$\hat{h}_2(q) = \hat{C}_2(q)(1 + n_0 \hat{h}_2(q)), \tag{8}$$

$$\hat{H}(\boldsymbol{q_1}, \boldsymbol{q_2}) = \hat{C}_3(\boldsymbol{q_1}, \boldsymbol{q_2}) G(\boldsymbol{q_1}, \boldsymbol{q_2}), \tag{9}$$

where

$$G(\boldsymbol{q_1}, \boldsymbol{q_2}) \equiv (1 + n_0 \hat{h}_2(q_1))(1 + n_0 \hat{h}_2(q_2))(1 + n_0 \hat{h}_2(|\boldsymbol{q_1} + \boldsymbol{q_2}|)), \tag{10}$$

and $\hat{C}_3(q_1, q_2)$ represents the Fourier transform of $C_3(1,2,3)$ with 3 taken to be the origin of the coordinate system. Similarly, $\hat{H}(q_1, q_2)$ represents the Fourier transform of the function $H(1,2,3)$ defined by,

$$H(1,2,3) \equiv h_3(1,2,3) - h_2(1,2) - h_2(2,3) - h_2(1,3)$$
$$- [h_2(1,2)h_2(2,3) + h_2(1,3)h_2(3,2) + h_2(2,1)h_2(1,3)]$$
$$- n_0 \int d4 h_2(1,4) h_2(2,4) h_2(3,4), \tag{11}$$

where $h_3(1,2,3) \equiv g_3(1,2,3) - 1$. In summary, we now have the self-consistent set of HNC3 equations, Eqs. (6), (7), (8) and (9) to determine four unknown functions g_2, C_2, C_3 and g_3 or $g_1(3|1,2)$.

III. NUMERICAL STUDY OF THREE-BODY HNC THEORY

A. numerical calculation details

The solution of the integral equation such as the HNC equation has been usually obtained numerically. To this end, the iterative scheme, which is generally called the Picard method, is introduced [1]. This method can be applied to our HNC3 theory because of its similar structure to the HNC theory. The procedure used here is the following: (i)take as the initial direct correlation functions $C_{m,in}$ $(m = 2, 3)$ the ideal gas ones; (ii)calculate the functions h_2 and h_3 through the OZ relations (8) and (9); (iii)obtain the new functions $h_1(2|1)$ and $h_1(3|1,2)$ by calculating the right-hand side of Eqs. (6) and (7); (iv)calculate the new direct correlation functions $C_{m,out}$ from the h_1 functions obtained in the step (iii) through the OZ relations; (v)take the next input direct correlation functions as

$$C_{m,in}^{new} = (1 - \alpha_m)C_{m,in} + \alpha_m C_{m,out} \quad (m = 2, 3), \tag{12}$$

where α_m is the parameter denoting a mixing weight; (vi)iterate (ii)-(v) until convergence is achieved. In order to judge the convergence, we define the norms N_m $(m = 2, 3)$ as

$$N_m \equiv \frac{\| C_{m,out} - C_{m,in} \|}{\| C_{m,in} \|}, \tag{13}$$

and monitor their changes at each iteration.

The system considerd here is a one-dimensional (1D) liquid with the pairwise interaction $\phi(r) = \epsilon(\sigma/r)^{12}$. The units of length and temperature are taken as $l \equiv 1/n_0$ and $T^* \equiv (k_B T/\epsilon)(l/\sigma)^{12}$, respectively. Then the thermodynamic state of the system can be characterized by one variable T^*. We considered two thermodynamic states $T^* = 10000$ and 50000, where the radial distribution function is modelately oscillatory. Since we obtained similar results in both cases, we will show the result of only $T^* = 10000$ in this paper. Numerical calculation was carried out with $\alpha_2 = 0.01$ and $\alpha_3 = 0.1$ in Eq. (12), which were chosen empirically. We fixed the variable 1 at the origin of the coodinate from the invariance of Eqs. (6) and (7) under space translation. For convenience, the variables 2 and

3 are expressed by x and y so that the functions, for example, $g_2(1,2)$ and $C_3(1,2,3)$ will be expressed simply by $g_2(x)$ and $C_3(x,y)$, respectively. The variables x and y are considerd in the range $|x|, |y| \leq 10$ with 512 mesh-points, convenient for use of the fast Fourier transform (FFT) method.

In our previous approach, we could not achieve convergence in the calculation of C_3, whose norm N_3 was observed to increase after about 100 iterations [10]. The problem was that the C_3 could not keep its smooth structure in the course of iteration due to accumulation of numerical errors. The errors turn out to come mainly from the use of the two-dimention discrete Fourier transform. To eliminate this difficulty related to FFT, we here introduce the filter function $f(x,y) \equiv \exp(-x^2/a^2)\exp(-y^2/a^2)$ with a constant a. We multiply the $C_3(x,y)$ by the $f(x,y)$ with $a = 6$ at each iteration in order to make $C_3(x,y)$ a smooth function. Since the $C_3(x,y)$ is a localized function of x and y around the origin $(0,0)$ in the range $|x|, |y| \lesssim 1$, this procedure does not influence the shape of the $C_3(x,y)$.

In Fig. 1, we show the norm changes N_m for $T^* = 10000$ as an iteration step increases. It is seen in Fig. 1 that both N_2 and N_3 become the order of 10^{-6} after about 15000 iterations and the convergence is fulfilled. In Fig. 2 we compare $C_2(x)$ of the ideal gas with the one from the HNC3 theory. In Fig. 3, we also plotted $C_3(x,y)$ of the ideal gas (a) and from the HNC3 theory (b). For C_2 and C_3, the direct correlation functions of an ideal gas are seen to considerably 'grow up' in a similar way due to the pairwise interaction, leading to rather strong effective repulsion for small separation of particles.

B. results

We performed molecular dynamics (MD) simulations of a 1D liquid with 4000 particles and obtained $g_2(x)$ at $T^* = 10000$ [2]. In Fig. 4, we show $g_2(x)$ at $T^* = 10000$. It is well known and also shown here that the $g_2(x)$ from the HNC equation has a higher first peak and a more compressed structure than the experimental one. On the other hand, it is noted that the HNC3 theory gives better $g_2(x)$ with respect to the height of the first peak and the

phase of the oscillation.

This improvement of the $g_2(x)$ is attributed to the three-body effect, which is explicitly taken into account through the $B^{(2)}(x)$ in Eq. (6). In order to quantify the three-body effect, let us turn to the brigde function $B^{(2)}(x)$ and the convolution function $C^{(2)}(x)$ in Eq. (6). In Fig. 5, we plot the combination $C^{(2)}(x) + B^{(2)}(x)$ in Eq. (6) and $C^{(2)}(x)$ from the HNC theory and the potential term $\phi(x)/T^*$ for the purpose of comparison. From Fig. 5, we notice that the $C^{(2)}(x) + B^{(2)}(x)$ from the HNC3 thory is smaller than the $C^{(2)}(x)$ from the HNC theory at $x \simeq 0.5$ where a particle contacts with a core. This change induces the improvement of the $g_2(x)$ with respect to the height of the first peak. In addition to this, Fig. 5 shows that there is a moderate improvement as to the oscillation phase between the HNC3 and the HNC theories.

Finally we comment on the Kirkwood superposition approximation (SA) [14]. Kirkwood approximated the three-body correlation function as the product of the two-body correlation functions as

$$g_3(1,2,3) \simeq g_2(1,2)g_2(2,3)g_2(3,1). \tag{14}$$

One obtains the Born-Green equation for $g_2(x)$ by applying this approximation to the Yvon-Born-Green hierarchy [1]. Once this factorized approximation is employed, we can obtain the third-order direct correlation function by inserting the SA g_3 to the three-body OZ relation (9). We thereby have another self-consistent closure (HNC3+SA) consisting of Eqs. (6), (8), (9) and (14) without recourse to Eq. (7). It should be noted that the bridge function $B^{(2)}$ in Eq. (6) is calculated by the C_3 approximated with the SA. We carried out the numerical calculation of the HNC3+SA with the iterative method explained before. In Fig. 6, we show the $g_2(x)$ at $T^* = 10000$ for the HNC3+SA, HNC, and MD, which indicate that the HNC3+SA theory improves the HNC theory similarly but slightly to less extent as the HNC3 theory does.

IV. CONCLUSIONS

In this paper, we discussed the HNC3 theory derived before based on the three-body DFT and the Percus' idea. We solved rather complicated set of equations, which consists of Eqs. (6), (7), (8) and (9), to determine the two- and three-body correlation functions self-consistently. For the 1D soft-rod system the HNC3 theory was shown to improve the HNC theory with respect to the height of the first peak and the phase relations of $g_2(x)$. Effects on the radial distribution function of the third-order direct correlation function C_3 were discussed through the convolution and bridge functions.

It should be noted that the system considered in the present work is at rather high (low) temperature (density). Furthermore, we studied only a 1D system in our numerical calculations. Numerical studies of the HNC theory for a 3D system seems to be a real challenge, which is worthwhile because three-body correlations play important roles in a dense fluid like a supercooled liquid or a glass. We hope that the M-body DFT will also lead to new insights into classical many-body problems.

REFERENCES

[1] J. P. Hansen and I. R. McDonald, *Theory of Simple Liquids* (Academic Press, 1986).

[2] M. P. Allen and D. J. Tildsley, *Computer Simulations of Liquids* (Clarendon Press, Oxford, 1987).

[3] J. M. J. van Leeuwen, J. Groeneveld, and J. de Boer, Physica **25**, 792(1959); T. Morita, and H. Hiroike, Progr. Theor. Phys. **23**, 1003 (1960).

[4] For reviews, see A. D. J. Haymet Annu. Rev. Phys. Chem. **38**, 89 (1987); D. W. Oztoby, in *Liquid, Freezing, and the Glass Transition*, edited by J. P. Hansen, D. Levesque, and J. Zimm-Justin (Elsevier, New York, 1990).

[5] A. D. Haymet and D. W. Oxtoby, J. Chem. Phys. **74**, 2559 (1981); D. W. Oxtoby and A. D. Haymet, *ibid.* **76**, 6262 (1982).

[6] Y. Singh, J. P. Stoessel, and P. G. Wolynes, Phys. Rev. Lett. **54**, 1059 (1985).

[7] D. Chandleer, J. D. Mccoy, and S. J. Singer, J. Chem. Phys. **85**, 5971 (1986); T. Munakata, S. Yoshida, and F. Hirata, Phys. Rev. E **54**, 3687 (1996).

[8] J. Percus, in *The Equilibrium Theory of Classical Fluids*, edited by H. L. Frisch and J. L. Lebowitz, (Benjyamin, New York 1964).

[9] L. Verlet, Physica **30**, 95 (1964); *ibid.* **31** 959 (1965).

[10] T. Munakata and K. Kim, J. Chem. Phys. **113**, 3975 (2000).

[11] J. L. Barrat, J. P. Hansen, and G. Pastore, Phys. Rev. Lett. **58**, 2075 (1987)

[12] P. Attard, J. Chem. Phys. **93**, 7301 (1990).

[13] E. Lomba, S. Jorge, and M. Álvarez, Phys. Rev. E **63**, 011203 (2000).

[14] J. G. Kirkwood, J. Chem. Phys. **3**, 300 (1935).

FIGURES

FIG. 1. The norm variation as a function of iteration steps for C_2 (solid curve) and C_3 (dashed curve).

FIG. 2. The second-order direct correlation function $C_2(x)$ at $T^* = 10000$ from the HNC3 theory (solid curve) and for an ideal gas (dashed curve).

FIG. 3. The third-order direct correlation function $C_3(x, y)$ at $T^* = 10000$ from the HNC3 theory (a) and for an ideal gas (b).

FIG. 4. The radial distribution function $g_2(x)$ at $T^* = 10000$ from the HNC3 theory (solid curve), the HNC theory (dashed curve), and MD simulation (closed circles).

FIG. 5. $C^{(2)}(x) + B^{(2)}(x)$ (solid curve) from the HNC3 theory, $C^{(2)}(x)$ (dashed curve) for the HNC theory, and the potential term $\phi(x)/T^*$ (dotted curve).

FIG. 6. The radial distribution function $g_2(x)$ at $T^* = 10000$ from the HNC3+SA theory (solid line), the HNC theory (dashed line), and MD simulation (closed circles).

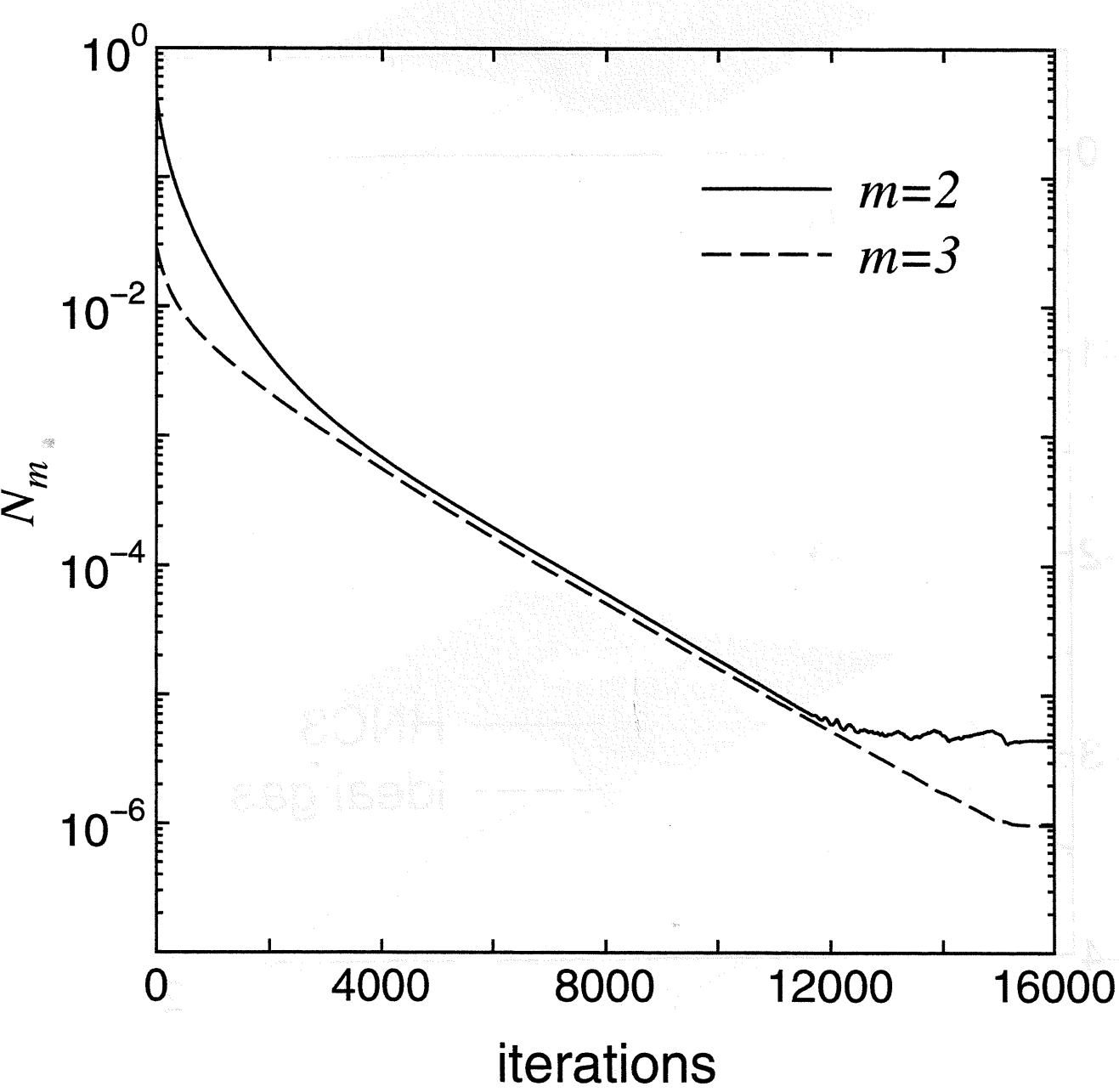

K. Kim FIG.1

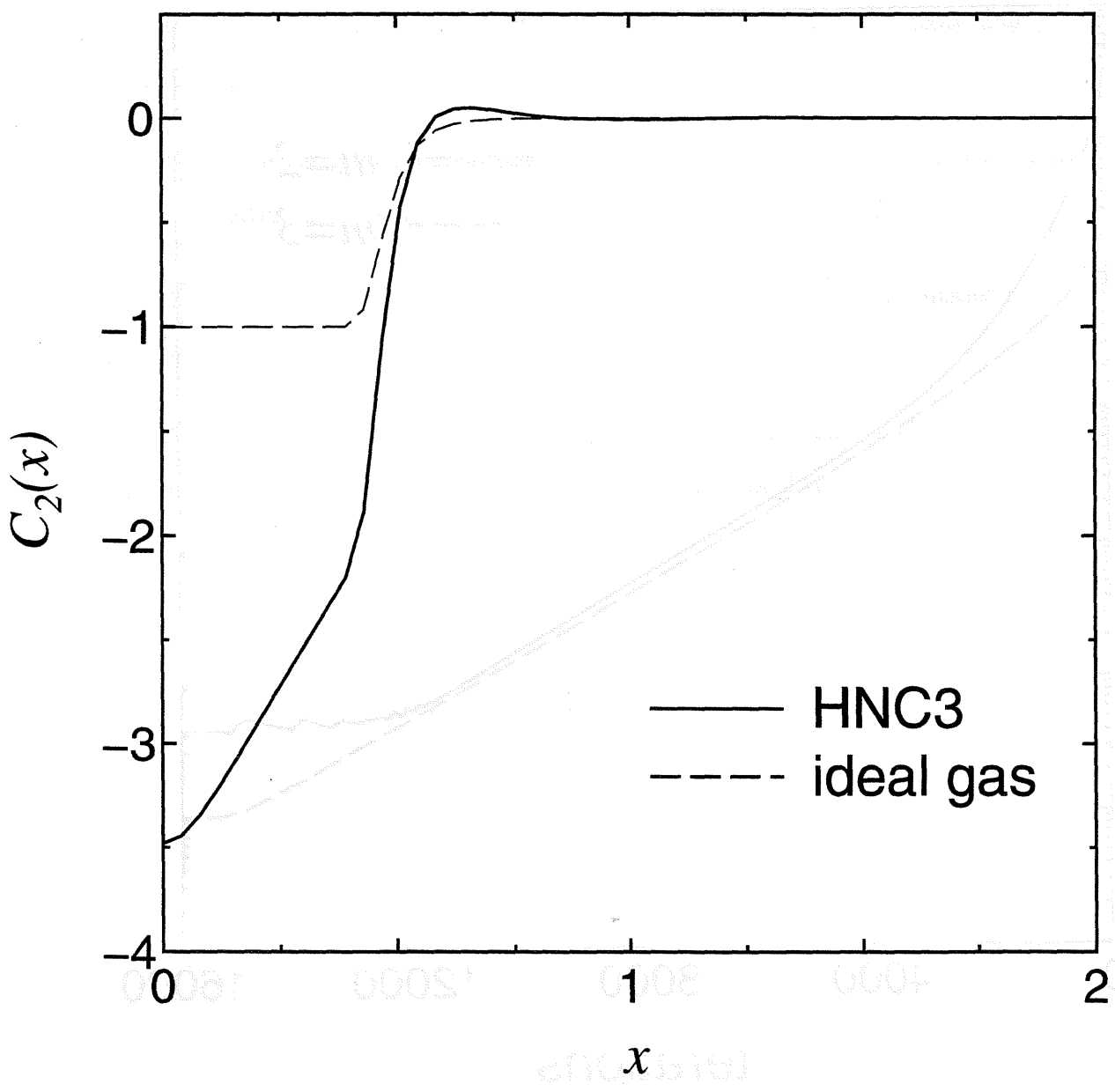

K. Kim FIG.2

(a) ideal gas

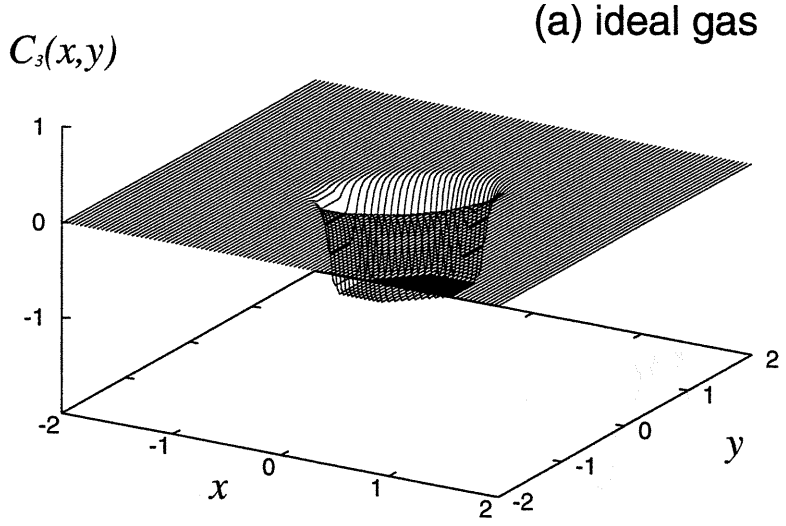

(b) HNC3

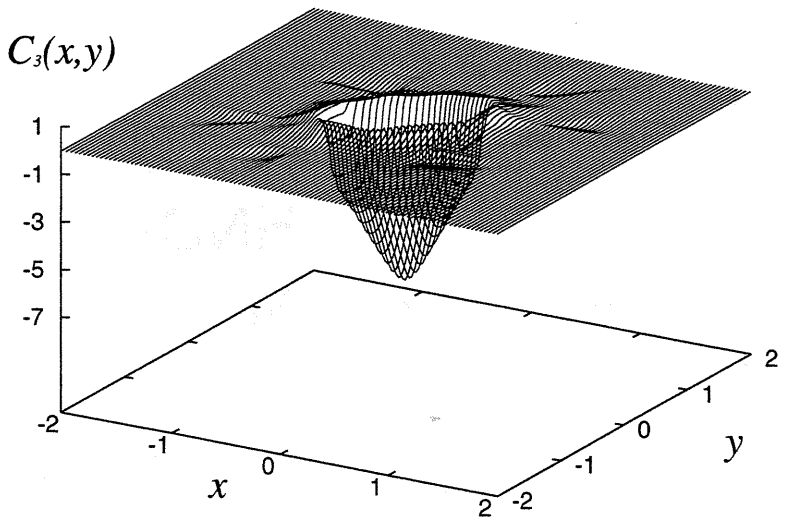

K. Kim FIG.3

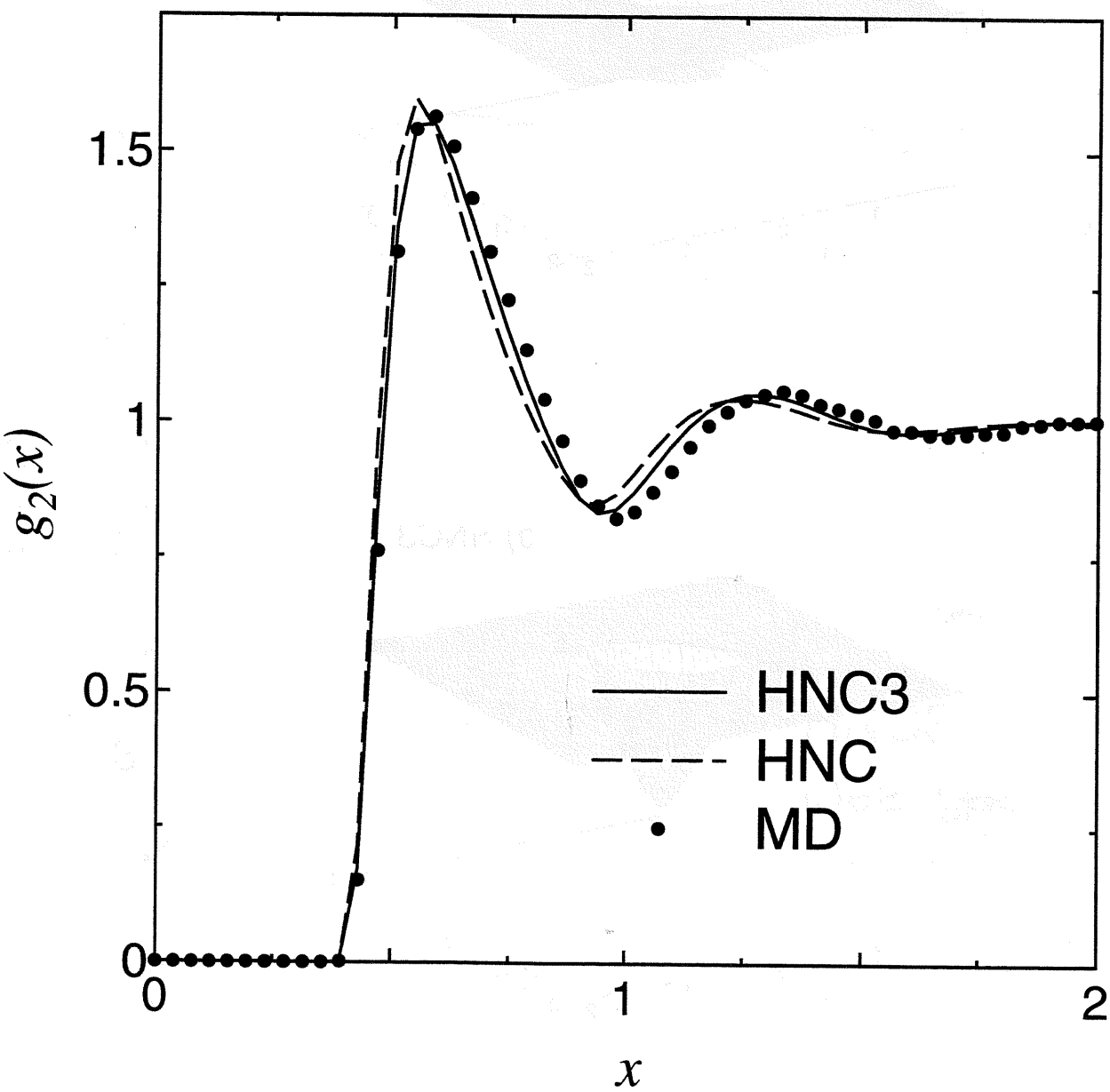

K. Kim FIG.4

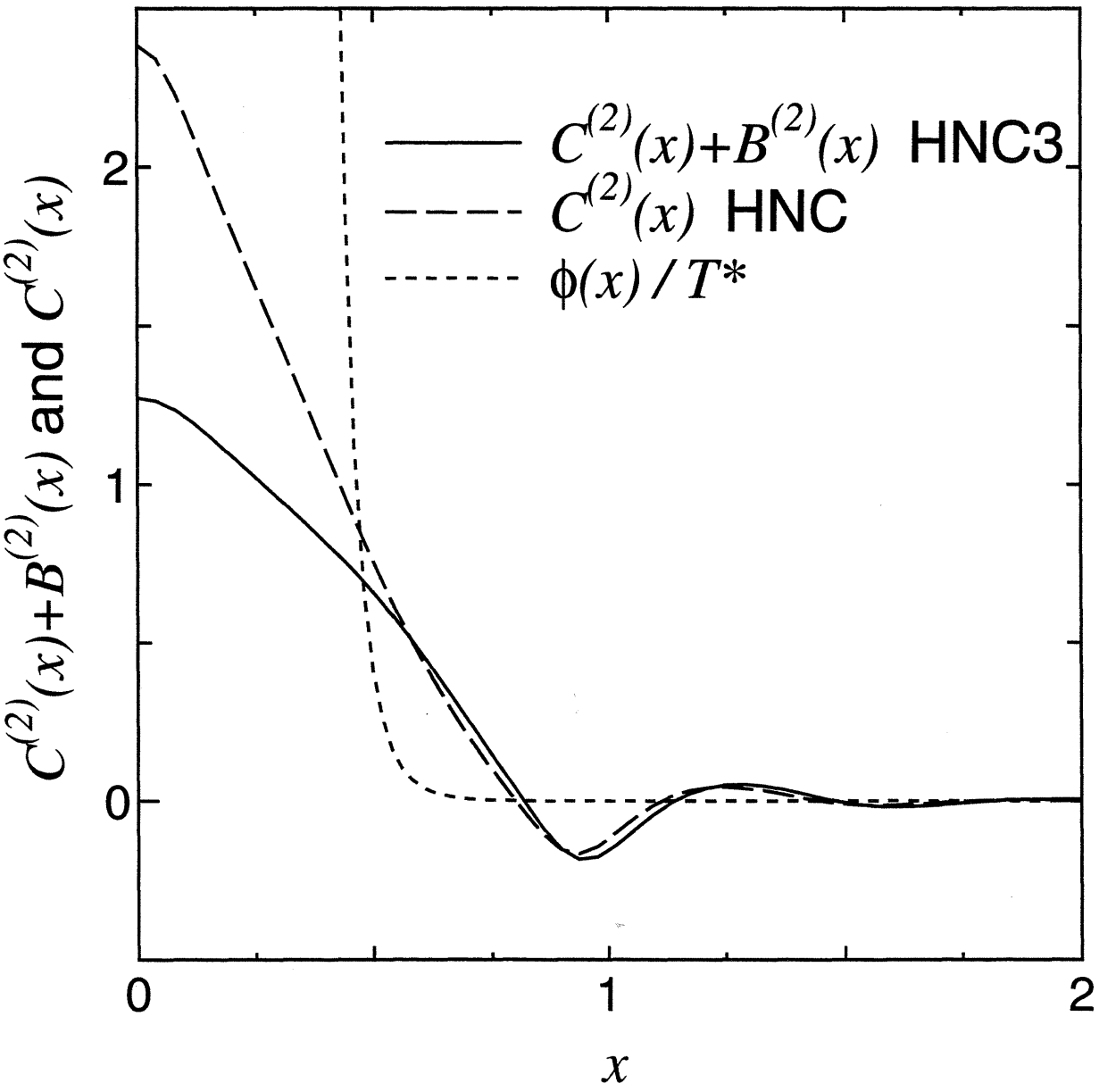

K. Kim FIG.5

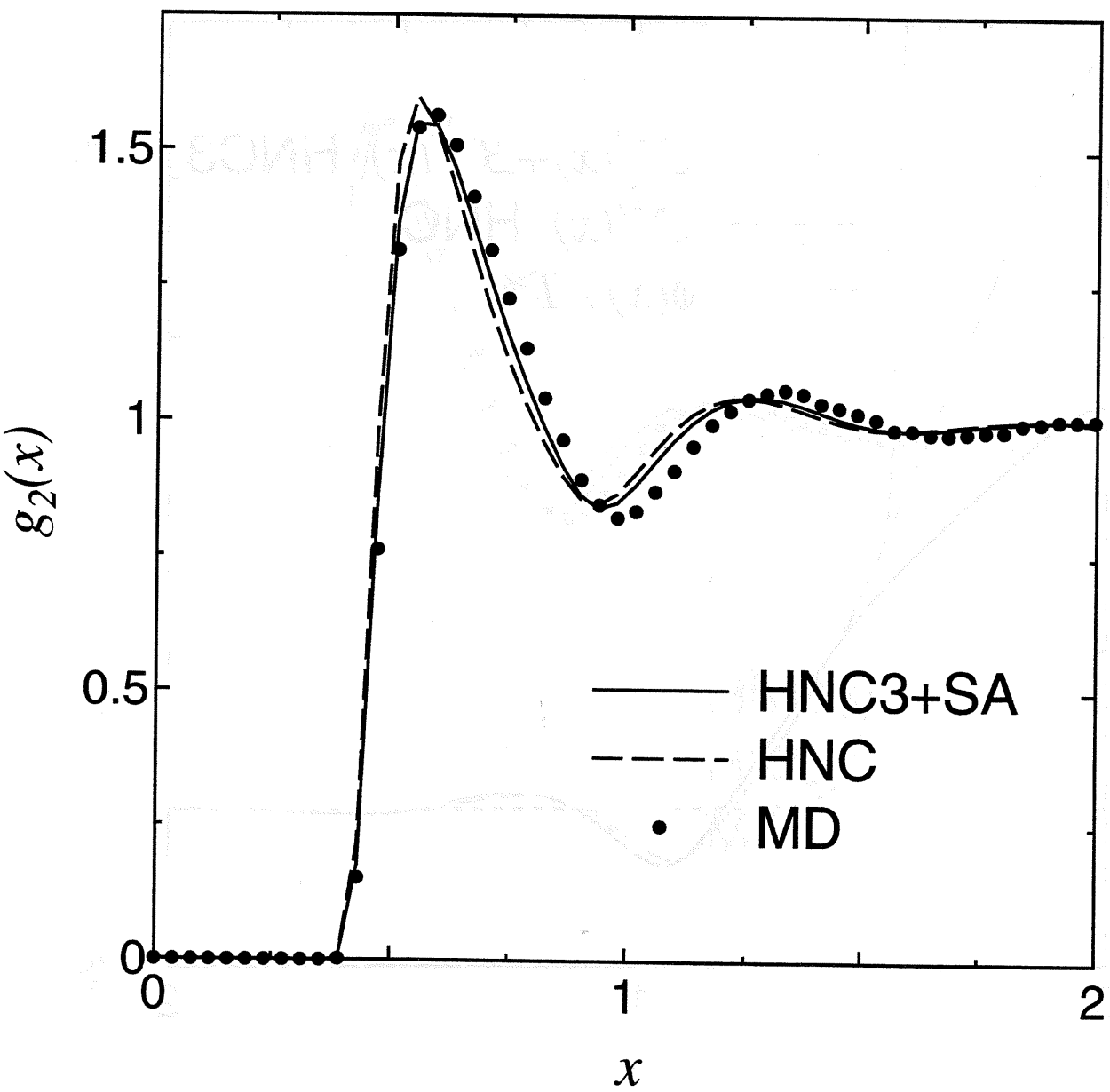

K. Kim FIG.6